Investigation of Electron Current Oscillations in the Plasma of a 5 kW-Class Hall Thruster Running on Xenon and Krypton

Vincent Delbosq, Stéphane Mazouffre

Investigation of electron current oscillations in the plasma of a 5 kW-class Hall thruster running on xenon and krypton

V. Delbosq* and S. Mazouffre†
CNRS, ICARE laboratory, Orléans, France

This contribution presents the examination of electron current time-series acquired in the plasma of the 5 kW-class PPS® Dual Hall thruster fired with xenon and krypton. The thruster was fired with xenon and krypton as propellant over a broad range of discharge voltages [250–600 V] and input powers [2.5–6 kW] in the PIVOINE-2G vacuum chamber. Time-resolved electron current measurements have been performed in the far-field plume with a cylindrical Langmuir probe polarized above the plasma potential to capture the whole electron population. A high-sensitivity calibrated current probe was used to directly measure the electron current with a 100 MHz sampling rate. Analysis of the electron current time-series and associated discharge current traces has been carried out with various tools: the Fourier transform, the wavelet transform and the Huang-Hilbert transform. The study reveals the impact of the applied voltage, the power and the propellant on different oscillation modes, namely the breathing mode, the ion transit-time mode and the high-frequency modes. It also shows similarities and discrepancies between the electron current dynamics and the discharge current dynamics. Finally, correlations between the various modes are explored.

I. Nomenclature

A	=	Surface area, m^2
d	=	Diameter, m
φ	=	Phase, rad
ω, f, ξ	=	Frequency, Hz
Φ_a	=	Anode mass flow rate, mg/s
Φ_c	=	Cathode mass flow rate, mg/s
I_c, I_d	=	Coil, discharge current, A
I, I_i, I_e	=	Total, ion, electron current, A
l	=	lenght, m
p, P	=	Pressure, Power, Pa, W
r, R	=	Radius, Thruster–probe distance, m
R_c	=	Probe circuit resistance, Ω
T	=	Thrust, N
U_d	=	Discharge voltage, V
V, V_s	=	Potential, probe potential, V
V_f	=	Floating potential, V
V_p	=	Plasma potential, V
x, y, z	=	Coordinates, m

*Research Engineer, CNRS, vincent.delbosq@cnrs-orleans.fr.
†Research Director, CNRS, stephane.mazouffre@cnrs.fr.

II. Introduction

Electrons play a key role in the physics of Hall thrusters as they govern to a large extend the ionization process through collisions with neutrals and the acceleration process through the electric field distribution. Collecting data about electron parameters such as the electron density and the electron temperature is therefore crucial to understanding how a Hall thruster works, to optimize thruster architecture, to develop new products and to validate physical models and numerical simulation outputs. Another relevant point in the understanding of Hall thruster physics is the electron dynamics. In fact oscillations in electron properties play an important role in thruster discharge stability, thruster performances and thruster lifetime. This is why studies of the temporal evolution of the electron density and temperature in the plasma and the plume of Hall thrusters have been carried out in the past, however mostly at the breathing mode time scale [1–4].

In this work we propose to examine the electron current, or electron current density, fluctuations in the course of time instead of focusing on electron parameters [5]. Thus, a small cylindrical Langmuir probe placed in the far-field region at 705 mm from the exit plane of the thruster has been used to capture the electron current. Firstly, studies on the electron current dynamics have been relatively neglected up to now, even though it provides information on the local plasma behavior, unlike the discharge current, which gives information on the averaged or integrated behavior of the plasma. Secondly, current oscillations are examined over a very wide range of frequencies, from kHz to MHz, making it possible to study various types of oscillatory modes and instabilities, not only the breathing mode. Thirdly, current oscillations are observed over a relatively long period of time, of the order of a tenth of a second, enabling us to study the phenomenon of intermittency and the unsteady nature of the oscillations. Finally, the range of power that is investigated here is broad, from 2.5 kW up to more than 6 kW and the thruster not only operates with xenon as propellant but also with krypton as the latter appears as a credible alternative. Experipments have been performed with the 5 kW-class PPS®Dual Engineering Model Hall thruster in the PIVOINE-2G vacuum chamber in Orléans, France. The latter was fired with xenon and krypton as propellant in both high-thrust / low-specific impulse and low-thrust / high-specific impulse regimes.

III. Vacuum chamber and Hall thruster

A. Hall thruster

1. Hall thruster and instabilities

Hall thrusters have emerged as a leading propulsion technology due to their proven effectiveness and reliability, as evidenced by their use in the Starlink satellite constellation. The Hall thruster is a gridless ion accelerator with a ring-shaped design and coils or permanent magnets at its center and periphery. Ion generation begins with a propellant, e.g. xenon, introduced through the anode. This propellant is ionized by high-energy electrons and confined within a ceramic annular channel, to allow a closed electron drift configuration. The majority of the resulting ions carry a single positive charge, with a noticeable proportion of doubly charged ions, as noted by S. Tsikata, I. Katz, and S. Kim [6–8]. Once generated, the ions are accelerated by a strong electric field (E) and expelled, reaching speeds of 20 to 30 km/s depending on the strength of the E field. This ion velocity generates thrust through momentum conservation. To ensure the electrical neutrality in the ion beam, a neutralizer is present.

The neutralizer supplies electrons to neutralize the ion beam and sustain the plasma discharge within the channel. In most cases, the neutralizer is a hollow cathode, fed with a small fraction of the propellant gas. Electron production is enhanced by a LaB_6 solid emitter. Electrons traveling toward the anode encounter a radial magnetic field, which confines them and enables efficient gas ionization. The magnetic field must ensure that the Larmor radius of the electrons remains smaller than the dimensions of the dielectric channel, while having no impact on the ions. At the Hall thruster exit plane, electrons are trapped in orbit around the magnetic field lines and the electron mobility transverse to the B field lines decreases sharply. To maintain the electron current (I_e), an intense axial electric field of several 100 V/cm [9] appears at the exit plane of the thruster, as the applied potential difference is concentrated in the region where the electrons are slowed down.

The presence of the electric field and magnetic field perpendicular to each other generates a strong azimuthal electron current, known as the Hall current, in the dielectric channel. This leads to highly efficient propellant ionization (90% with X_e). Extensive researchs on this class of thruster have highlighted a broad spectrum of instabilities spanning frequencies from kHz to GHz, capable of inducing transient oscillatory phenomena or turbulence [10, 11]. It is important to emphasize that not all oscillations adversely impact thruster performance; plasma and discharge instabilities are

integral to key processes such as propellant ionization and ion acceleration. Among this, the breathing mode represents the predominant instability in Hall thrusters within this frequency range. The main oscillations [12] in a Hall thruster are as follows:

- Low frequency ionization oscillations: Breathing mode [13], 10 - 20 kHz range. The instability is distinctly characterized by the discharge current and is significantly influenced by factors such as the channel material, magnetic field, discharge voltage, and gas flow rate. Its name originates from the periodic nature of neutral ionization and ion expulsion from the channel, drawing an analogy to breathing, whereby air is inhaled, and carbon dioxide is exhaled.
- Azimutal low frequency oscillations (kHz range).
- Axial ion transit time oscillations: 100 - 500 kHz range. This frequency range coincides with the inverse of the time of flight required for the ions to traverse the acceleration zone, which extends aproximately a few centimeters from the exit plane of the thruster.
- High-frequency instabilitiy (e.g. $E \times B$ electron drift): 1 - 10 MHz range. Electron Drift Instability is specific to Hall thrusters but is more broadly referred to in the literature as the electron cyclotron drift instability. The latter arises from the coupling of the electron Bernstein modes with ion acoustic modes. Its existence has been confirmed through the use of two-dimensional particle-in-cell simulations and further corroborated by means of collective light scattering experiments.

2. PPS®Dual thruster

The PPS®Dual thruster is a 5 kW-class Hall thruster developed by SAFRAN. The PPS®Dual thruster is able to deliver both a large thrust level and a large specific impulse I_{sp} level at high power, up to 7 kW. The unique dual mode capability of the PPS®Dual rests upon a highly versatile magnetic configuration that inherits the experience gained with the PPS®1350, the PPS®5000 and the PPS 20k-ML thrusters over the last decade. A high thrust is for instance required for orbit raising and orbit transfer in order to reduce the maneuver duration. A large specific impulse is preferable for station keeping and trajectory corrections in the case of satellites. For cargo vehicles, space tugs and interplanetary missions a large I_{sp} makes it possible to considerably reduce the propellant mass and therefore increase the payload mass or extend velocity increment capacity. Two main input power targets have been initially proposed with xenon as fuel for the PPS®Dual thruster to cover aforementioned needs, namely: a 7 kW operating point for high thrust (0.5 N,$I_{sp} \geq 1800$ s, $T/P = 72$ mN/kW) and a 3.5 kW operating point for large specific impulse (0.2 N,$I_{sp} \geq 2100$ s, $T/P = 57$ mN/kW).

Two versions of the PPS®Dual thruster have been developed in the frame of the European CHEOPS project: a laboratory version, termed LM, and an engineering model, termed EM. In this work, the EM version was used with xenon and krypton as propellants. A photograph of the EM version of the PPS®Dual thruster is shown in Fig. 1a. As can be seen, the LaB_6 hollow cathode that furnishes the electron current for plasma discharge generation and ion beam neutralization is positioned under the thruster body. The thruster channel is dimensioned to warrant stable and efficient operation around 5 kW input power. Channel walls are made of boron-nitride ceramics (BN). The propellant gas is injected from the channel back through an annular graphite injector that also serves as anode. The magnetic field is created by a set of magnetizing coils (4 external coils,1 inner coil and 1 back coil) embedded into a pure iron magnetic circuit. The magnetic design gives a large flexibility in terms of shape and magnitude. Figure 1b shows the PPS®Dual-EM thruster in operation with krypton at 5 kW in the PIVOINE-2G test bench. As can be seen, the plasma discharge is concentrated in the ceramic channel. The cathode plasma plume is also visible in Fig. 1b.

3. Operating conditions

The PPS®Dual Hall thruster was operated over a broad range of discharge voltages and currents during the experimental campaign. Several investigations were conducted on both the discharge current and the electron current. In the first part of the study, the spectral evolution was examined as a function of either the discharge voltage or the gas flow rate, with one parameter held constant in each case. In the subsequent phase, insights from the initial analysis were used to determine optimal conditions for applying a wavelet transform and then a Huang-Hilbert transform, enabling a time-resolved investigation of instabilities. The cathode mass flow rate - Φ_c - was set to 8 % of the anode flow rate for all conditions. The residual gas pressure in the vacuum chamber remained roughly at the same pressure, i.e. [1.10^{-5} – 2.10^{-5}] mbar.

Operating parameters for the broad spectrum analysis are listed in Table 1 for the discharge voltage study and in Table 2 for the mass flow rate study. Six operating conditions [OP1 – OP6] have been selected for performing wavelet

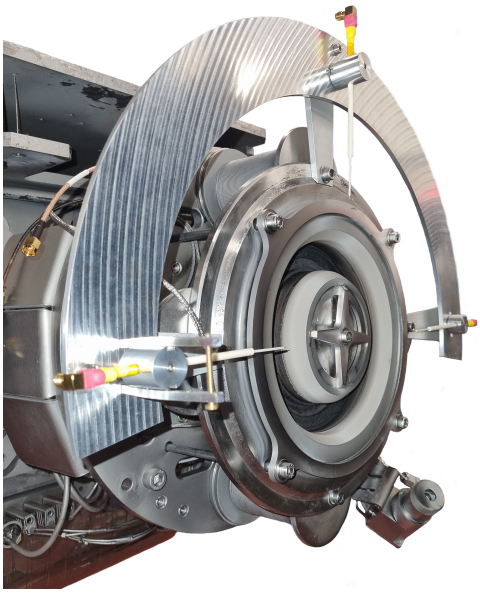

(a) PPS®Dual-EM thruster.

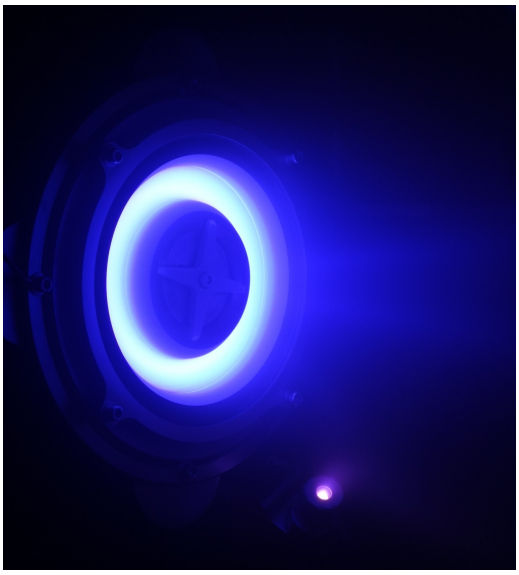

(b) PPS®Dual-EM thruster firing with krypton.

Fig. 1 (a) Photograph of the high-power PPS®Dual-EM Hall thruster installed on the PIVOINE-2G test-bench thrust balance. (b) Photograph of the PPS®Dual-EM Hall thruster firing with krypton in the PIVOINE-2G test-bench.

Table 1 Operating conditions of the PPS®Dual-EM thruster with xenon and krypton, analyzed across multiple discharge voltages for broadband spectrum characterization.

Gas	Φ_a	U_d	P
-	mg/s	V	kW
X_e	10.0	[250 – 500]	[2.6 – 5.17]
K_r	8.0	[250 – 500]	[2.54 – 5.36]

analysis and are listed in Table 3 for xenon and in Table 4 for krypton.

B. The PIVOINE-2G test bench

Investigation of the high-power PPS®Dual Hall thruster plasma plume properties has been performed in the PIVOINE-2G test-bench at the ICARE laboratory in Orléans. This ground-test facility is fully dedicated to research and development activities in the field of Electric Propulsion. PIVOINE-2G is a cryogenically pumped 4 m in length and 2.2 m in diameter stainless steel vacuum chamber. The bench allows testing Hall thrusters from 100 W up to 25 kW input power. The PIVOINE-2G test-bench was built in 1997 with the financial support of the French space agency CNES and the "Region Centre Council". It was upgraded in 2007 to achieve a pumping speed in excess of 250000 l/s, one of the largest within Europe. The current version is composed of two cryogenic stages optimized for xenon, although krypton and argon can also be efficiently evacuated. The cryogenic panels are shielded from the thruster thermal load and from the ion beam by means of LN_2 cooled graphite tiles. When using the two stages, a background gas pressure of 2×10^{-5} mbar can be achieved with 20 mg/s of xenon. A 2000 l/s-N_2 turbomolecular pump is also used for removal of light gases like hydrogen and helium. The vacuum chamber is equipped with a large lock-chamber that permits inserting the thruster without disturbing the vacuum as well as with different observation windows and diagnostic ports. PIVOINE-2G has a set of diagnostics that includes a thrust balance, ion current probes and an energy analyzer. The probes can be installed either on a 2D translation stage or on a rotating arm that allows performing measurements in a hemisphere. The thrust balance is a pendulum stand, calibrated in-situ with a series of weights. The estimated

Table 2 Operating conditions of the PPS®Dual-EM thruster with xenon and krypton, analyzed across multiple gas flow rates for broadband spectrum characterization.

Gas	Φ_a	U_d	P
-	mg/s	V	kW
X_e	[5 – 12]	300	[1.45 – 3.7]
X_e	[5 – 12]	400	[2.0 – 5.0]
X_e	[5 – 12]	450	[2.3 – 5.58]
K_r	[5 – 10]	300	[1.65 – 3.92]
K_r	[5 – 10]	400	[2.27 – 5.42]
K_r	[5 – 10]	450	[2.63 – 6.45]

Table 3 Operating conditions of the PPS®Dual-EM thruster for xenon.

Point	Φ_a	U_d	I_d	P
-	mg/s	V	A	kW
OP1	10.0	280	10.25	2.87
OP2	10.0	300	10	3
OP3	10.0	360	9.92	3.57
OP4	10.0	430	9.98	4.29
OP5	10.0	450	10.44	4.7
OP6	10.0	500	10.34	5.17

accuracy of the measured thrust is ±1 mN for a thrust ranging from 5 to 1500 mN. The discharge power is provided by two 500 V – 30 A power supplies mounted either in parallel or in series. During operation of a thruster, more than hundred parameters are monitored and continuously acquired. In 2019, the PIVOINE-2G bench control unit has been upgraded to allow fully automated operation and process. The facility is now able to operate on a 24 hour/7 day basis, which reduces cost and duration of endurance testings and open up the way to more ambitious experimental campaigns.

IV. Measuring instruments

A. Langmuir probe and current probes

A cylindrical Langmuir probe was built to assess the electron current in the plasma plume of the PPS®Dual Hall thruster, see [14–21]. Figure 2 shows the layout of the Langmuir probe. The probe, is placed in the far downstream region of the plasma plume r = 705 mm away from the channel exit plane. The latter is mounted onto a rotating arm in order to perform measurements over a 200° circular arc. Note the probe is in the horizontal plan that contains the thruster centerline. The probe tip points towards the thruster axis. The pivot point of the rotating arm is in the thruster channel exit plan and aligned with the thruster axis. In this study, we only focused on the electron current collected on the thruster centerline.

The probe tip geometry made in tungsten is adjusted in such a way the plasma sheath thickness in the surveyed region is much below the tip length to minimize local perturbations of the plasma [22–27]. The non-active section of the W wire was shielded from the plasma with a 1.5 mm outer diameter alumina tube inserted into a shorter 2 mm inner diameter alumina tube, as illustrated in Fig. 1a. The total length of the probe was 100 mm. A 50 Ohms coaxial cable was used to polarized the probe and collect the current. The voltage applied to the probe, typically around 70 V, the ground of the vacuum chamber being used as the reference, was always above the local plasma potential in order to collect the whole electron population, or in other words to capture the whole EEDF. The electron current was directly measured with a high-sensitivity calibrated CP031A probe (30 A peak) and the thruster discharge current was measured by means of a calibrated AP015 probe (50 A peak) from Teledyne Lecroy. The two probe types are based on a combination of

Table 4 Operating conditions of the PPS®Dual-EM thruster for krypton.

Point	Φ_a	U_d	I_d	P
-	mg/s	V	A	kW
OP1	8.0	250	10.16	2.54
OP2	8.0	350	10.17	3.56
OP3	8.0	400	10.4	4.16
OP4	10.0	450	14.34	6.45
OP5	8.0	480	10.67	5.12
OP6	5.0	580	10.17	5.9

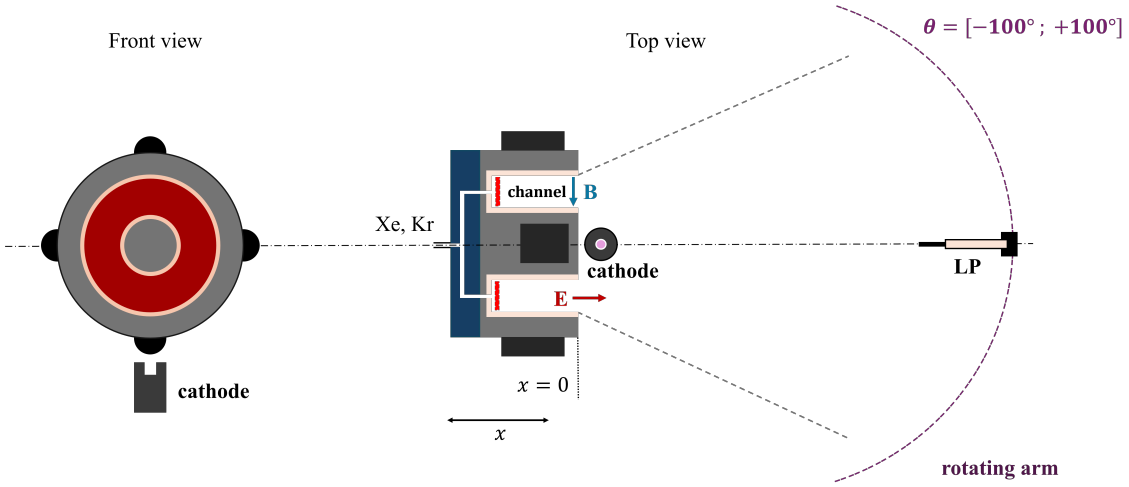

Fig. 2 Layout of the Langmuir probe. Not to scale.

Hall effect and transformer technology therefore enabling AC and DC current measurements. The CP031A probe, respectively AP015 probe, bandwidth is 100 MHz, respectively 50 MHz, above the largest frequencies of interest here ($\approx$ 10 MHz). Probes were connected to the 50 Ω input channels of a HD4096HDO6104A oscilloscope from Teledyne Lecroy. The latter has a 12-bit ADC resolution and 1 GHz bandwidth with a long memory. The sampling frequency was set to 100 MHz and the sample length was 100 ms, which corresponds to a number of samples of 10^7.

As previously mentioned, the probe was mounted onto a dedicated holder fixed to the PIVOINE-2G vessel rotating arm. A CAD image of the holder is given in Fig. 3. As can be seen, the Langmuir probe angular position does not coincide with the one of the rotating arm, hence making the measuring device asymmetrical. In other words, when the arm is placed at $\theta_{arm} = 0°$, the probe is at another angular position. The angle between the Langmuir probe and the arm is +15°.

B. Electron and discharge current time-series

Electron and discharge current time-series have been recorded for a broad range of discharge voltages [250 – 600 V] and input power [2.5 – 6 kW] with xenon and krypton as propellant. Electron and discharge current time-series data has been analysed in the frequency-domain using various time-frequency analysis techniques, namely: the Fourier transform, the wavelet transform (WT) and the Huang-Hilbert transform (HHT), which combines the Empirical Mode Decomposition with the Hilbert transform. The HHT decomposes a signal into so-called intrinsic mode functions and provides instantaneous frequencies. The tool performs particularly well with data that is nonstationary and nonlinear.

Fig. 3 CAD image of the Langmuir probe setup. The LP is not aligned with the rotating arm.

1. The Fourier transform

The primary goal of signal processing is to identify and extract information embedded within a given signal, irrespective of its form. For instance, a signal could represent a current described by a function s. Visually, the human brain can analyze such a signal over time, recognizing its onset, duration, and conclusion. It can also discern specific patterns and rhythmic fluctuations, such as discontinuities, narrowing, or widening. However, visual inspection alone cannot provide precise information about the periodicity of a signal, hence its frequency components.

In the 19$^{\text{th}}$ century, Fourier introduced a groundbreaking approach by decomposing signals into sums of sinusoidal signals, thereby revealing their underlying frequencies. Mathematically, the Fourier transform converts a time-domain function into a frequency-domain function, which represents its spectral content. For an integrable function s on $\mathbb{R}$, the Fourier transform is defined as:

$$\mathcal{F}(s) : \nu \rightarrowtail \hat{s}(\nu) = \int_{-\infty}^{+\infty} s(t) e^{-i2\pi\nu t}\, dt \tag{1}$$

where t is in secondes, ν in Hertz and $e^{i2\pi\nu t} = \cos(2\pi\nu\, t) + i\sin(2\pi\nu\, t)$, the Euler's Formula.

However, this continuous form of the Fourier transform cannot be directly applied to digital signals, which are represented by a finite number of samples. Instead, the discrete Fourier transform (DFT), or more commonly its computationally efficient counterpart, the fast Fourier transform (FFT), is used. Consequently, for a discrete signal $s(t)$ with N samples, the FFT yields:

$$S[k] = S(i\xi)\big|_{\xi=\frac{2\pi k}{N}} = \sum_{n=0}^{N-1} s[n] e^{-i2\pi k \frac{n}{N}}, \text{ for } 0 \leqslant (k, n) < N \tag{2}$$

where $(k,\, n) \in \mathbb{N}^2$. One of the key advantages of the Fourier transform is its general applicability. It does not require prior assumptions about the nature or the origin of the signal, making it an indispensable tool especially in the initial phase of investigating a signal, providing essential insights into the overall frequency behavior.

During the 1940s, both mathematics and signal processing continued to evolve, leading to the development of more advanced tools. One such innovation was the short-time Fourier transform, which introduced the first time-frequency representation of signals [28]. Despite its relevance, the short-time Fourier transform has notable limitations, primarily due to its fixed window length. This constraint makes it less effective for analyzing phenomena with varying periodicities. In 1983, J. Morlet addressed this limitation by introducing an improved technique. By incorporating a window with a variable length – capable of dilatation or contraction – this method provided a more versatile approach to time-frequency analysis. This marked the inception of wavelets.

2. The wavelet transform

A wavelet is a small, oscillatory wave with a clearly defined beginning and end. A mother wavelet serves as the foundation for representing a function – such as I_d and I_e – as a weighted sum of translated and scaled (dilated) versions

of the mother wavelet, referred to as child wavelets. This process, which generates a set of wavelet coefficients associated with the function under investigation, is known as the wavelet transform.

Wavelet transforms are widely utilized in various fields, including image processing (e.g., medical imaging) and the detection of gravitational waves for instance. However, their application to electric propulsion remains limited, as evidenced by the scarcity of research articles connecting the two fields. Indeed, we noted one article focused on the MHz range [29] and another one covering a broader range [4] that aligns with our research focus.

The selection of the mother wavelet is theoretically at the discretion of the researcher, provided it satisfies specific mathematical conditions. These conditions include:

- Square integrability in the Hilbert space $L^2(\mathbb{R})$,
- Oscillatory behavior, and a mean value of zero.

Additionally, the mother wavelet may be complex, providing greater flexibility in representations. Thus we defined a family $\psi_{\varsigma,\tau}(t)$, where $D(\psi) = \{(\varsigma, \tau) \in \mathbb{R}^{*+} \times \mathbb{R}\}$, of wavelets derived from the mother wavelet Ψ, as given by:

$$\forall\, t \in \mathbb{R},\ \psi_{\varsigma,\tau}(t) = \frac{1}{\sqrt{\varsigma}} \Psi\left(\frac{t-\tau}{\varsigma}\right) \tag{3}$$

If $s(t)$ is a real-valued function of a real variable, its wavelet transform is mathematically expressed as:

$$\mathcal{W}_s(\varsigma, \tau) = \int_{-\infty}^{+\infty} s(t)\, \bar{\psi}_{\varsigma,\tau}(t)\, dt \tag{4}$$

Thus, using Eq. (3), we get:

$$\mathcal{W}_s(\varsigma, \tau) = \frac{1}{\sqrt{\varsigma}} \int_{-\infty}^{+\infty} s(t)\, \bar{\Psi}\left(\frac{t-\tau}{\varsigma}\right) dt, \tag{5}$$

where ς is the scale parameter, the bar symbol refers to the complex conjugate and τ is the position parameter where the convolution is applied on a δt window.

The Morlet wavelet, formed by convolving a sinusoidal function with a Gaussian envelope, see Fig. 4, has been selected as the mother wavelet for this analysis. The Gaussian envelope minimizes the product of temporal and frequency resolutions of the wavelet, thereby optimizing the accuracy of time-frequency representations.

Two parameters, f_0 and β_b, are adjustable in the Morlet wavelet, see Eq. (6).

$$\psi_{f_o,\beta_b}(t) = \frac{1}{\sqrt{\pi\beta_b}} e^{i2\pi f_0 t}\, e^{\frac{-t^2}{\beta_b}} \tag{6}$$

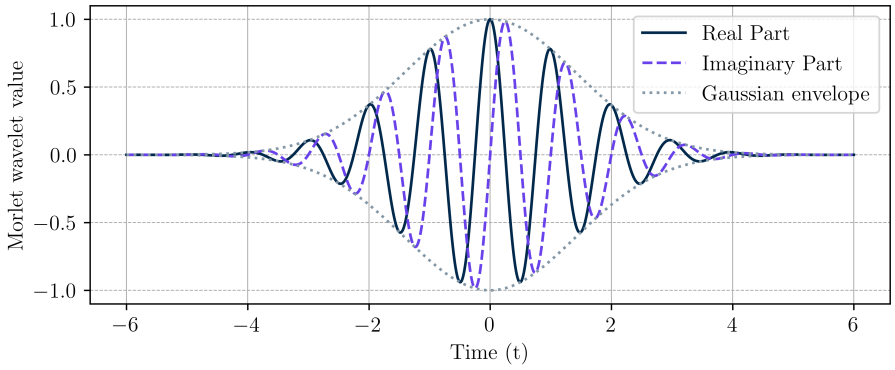

Fig. 4 Representation of the complex Morlet wavelet with $f_0 = 1$ and $\beta_b = 4$.

Careful consideration is required when selecting these parameters, as they significantly influence the results. It is common practice to set $f_0 = 1$ to preserve time-frequency correlation and enhance edge visibility. The width β_b, which controls the trade-off between frequency and time resolution, is typically chosen within the range of 3 to 6. After extensive testing across various combinations, $\beta_b = 4$, was determined to be the most appropriate value for this study. For additional details on wavelets and their associated transforms, readers are encouraged to consult the referenced literature [28, 30–33].

3. The Huang-Hilbert transform

The Huang-Hilbert transform (HHT), introduced by Norden E. Huang, is a powerful algorithm in signal processing, offering a time-frequency representation of non-stationary and non-linear data. This transformative approach is widely applied across various scientific fields, such as climatology, seismology, and biomedical imaging. By decomposing signals into multiple modes, the HHT provides critical insights into the amplitude and instantaneous frequency of each mode. Regarding Hall thruster physics, we noted one article in which the auhtors focused their investigation on the MHz range [34] and another one that explored a broader frequency range, spanning from kHz to MHz [39]. For a comprehensive description of the method, the reader is directed to the referenced literature [35–39]. Here, we provide only a brief summary to outline its main steps.

The HHT integrates two complementary methodologies. First, it employs the Empirical Mode Decomposition (EMD) technique, which differs fundamentally from Fourier or wavelet transforms by deriving its decomposition basis intrinsically from the signal itself. Through EMD, a signal is decomposed into $k \in \mathbb{N}^*$ Intrinsic Mode Functions (IMFs). Each IMF satisfies two criteria, namely: the number of extrema and zero crossings must either be equal or differ by at most one, and the mean value of the upper and lower envelopes must be zero.

Consider a signal $s(t)$, to which the EMD method is applied, resulting in:

$$s(t) = r(t) + \sum_{j=0}^{k} C_j(t),\ k \in \mathbb{N}^*, \tag{7}$$

where k is the number of intrinsic mode functions (IMFs), $r(t)$ is the residual component of the decomposition and $C_j(t)$ corresponds to the j$^{\text{th}}$ IMF. The following step of the HHT is the Hilbert Transform. The latter is applied to each IMF to compute the associated analytical signal $Z(t)$, represented as a combination of its real and imaginary components:

$$Z(t) = C_j(t) + i\mathcal{H}\{C_j(t)\} = A_j(t)e^{i\varphi_j(t)}, \tag{8}$$

where $A_j(t)$ represents the amplitude of $Z(t)$, and $\varphi_j(t)$ denotes the complex phase (i.e., the argument). The real part of $Z(t)$, $C_j(t)$, is defined as:

$$C_j(t) = IMF_j(t) = \mathbb{R}\{A_j(t)e^{-i\varphi_j(t)}\} = A_j(t)\cos(\varphi_j(t)). \tag{9}$$

The imaginary part of $Z(t)$, the Hilbert transform of $C_j(t)$, $\mathcal{H}\{C_j(t)\}$, is expressed as follows:

$$\mathcal{H}\{C_j(t)\} = \frac{1}{\pi}\,\text{p.v.}\int_{-\infty}^{+\infty}\frac{C_j(\tau)}{t-\tau}\,d\tau = \tilde{C}_j(t), \tag{10}$$

where p.v. stands for the Cauchy principal value. Following the determination of the real and imagnary components of $Z(t)$, the amplitude $A_j(t)$ is calculated as:

$$A_j(t) = \sqrt{C_j(t)^2 + \tilde{C}_j(t)^2}, \tag{11}$$

and the instantaneous frequency which is derived from the complex phase $\varphi_j(t)$, is expressed as:

$$\omega_j(t) = \dot{\varphi}_j(t) = \frac{d\varphi_j(t)}{dt} = \frac{d}{dt}\arctan\left(\frac{\tilde{C}_j(t)}{C_j(t)}\right). \tag{12}$$

The amplitude $A_j(t)$, instantaneous frequency $\omega_j(t)$, and time t form a set of triplets [t, $\omega_j(t)$, $A_j^2(t)$], which then constitutes the Hilbert power spectrum, $H(\omega_j, t)$, of each mode. Afterward, the final step consists of determining the marginal spectrum, $h(\omega)$, obtained by integrating the Hilbert spectrum of each IMF$_j$ over time. The latter is defined as follows:

$$h(\omega) = \int_0^T H(\omega, t)\,dt, \tag{13}$$

where T is the total length of the signal s. This marginal spectrum yields a frequency distribution of the signal amplitude, whereas the Hilbert spectrum presents a frequency-time distribution of the signal amplitude.

V. Plasma oscillations in the plume far-field

A. Electron and discharge currents frequency domain analysis for both xenon and krypton

1. As a function of the discharge voltage

This section details the findings on the evolution of discharge current and electron current oscillations in response to variations in plasma discharge parameters. The initial analysis investigates the impact of discharge voltage on plasma oscillations (see Table 1).

Figure 5 and Fig. 6 present the operational characteristics of the thruster as a function of U_d when fired with a xenon flow rate of 10 mg/s and a krypton flow rate of 8 mg/s, respectively. These figures detail the standard deviation, extremum values, and breathing mode (BM) frequency for both the discharge current and the electron current. For the discharge current obtained with xenon in Fig. 5a, the standard deviation is notably high around 300 V, followed by a marked decrease up to 430 V, before rising again at higher discharge voltages. This behavior is consistent with the BM frequency evolution. This is also confirmed by the electron current caracteristics in Fig. 5b, albeit a 10 kHz difference in the BM frequency was noticed at high voltage between the electron current and the discharge current. Thus, for xenon we can assume four regimes as follows:

- Regime A: $U_d < 330$ V, I_d decreases and σ fluctuates.
- Regime B: $330 < U_d < 420$ V, I_d is constant and oscillations are low.
- Regime C: $420 < U_d < 440$ V, transition zone.
- Regime D: $U_d > 440$ V high dispersion, higher I_d and jump in the breathing mode.

In Fig. 6a, with krypton, the breathing mode exhibits a quasi-linear progression with increasing discharge voltage. Additionally, the standard deviation shows a gradual increase across the voltage range starting from 280 V. This is also confirmed in Fig. 6b by the electron current caracteristics. Hence, for krypton we can distinguish two regimes:

- Regime A: $U_d < 280$ V, I_d decreases.
- Regime B: $U_d > 280$ V, I_d increases.

It can thus be concluded that the frequency of the breathing mode is significantly influenced by the discharge voltage, independent of the gas or flow rate used.

In order to characterize the frequency behavior of the signal at each voltage step, the Fourier transform was applied using the FFT algorithm. To enhance continuity and achieve an effective graphical representation, the FFT results were extrapolated between consecutive voltage steps (e.g., 250 V and 260 V). The extrapolation employed the Gouraud shading technique for a two-dimensional visualization, implemented using Python. Amplitude data for each frequency component in the FFT was expressed in decibels (dB), calculated using the relation $A(\text{dB}) = 20\log_{10}\left(\frac{I}{I_0}\right)$, where I represents the signal intensity and I_0 is the reference intensity. To improve readability and reduce noise without distorting the results, the amplitude was subsequently smoothed using the Savitzky-Golay algorithm with optimized parameters (100, 9).

Figure 7 illustrates the frequency evolution of I_d (Fig. 7a) and I_e (Fig. 7b) as functions of U_d for xenon, measured at a flow rate of 10 mg/s, presented as a two-dimensional contour plot. Similarly, Fig. 8 displays the frequency evolution of I_d (Fig. 8a) and I_e (Fig. 8b) as functions of U_d for krypton, measured at a flow rate of 8 mg/s, also in two-dimensional contour format. The frequency ranges analyzed for I_d and I_e span from kilohertz to 10 MHz and from kilohertz to 1 MHz, respectively. The reduced frequency range for I_e reflects interference with the Langmuir probe, caused by a power supply beyond the megahertz range.

Analysis of the spectra indicates that the breathing mode frequency increases with discharge voltage, starting at 10 kHz and reaching 20 kHz, while its amplitude attenuates within the voltage range of 320 – 420 V. However, when operating with xenon, the frequency transitions are sharp, as the one observed around 430 V, corresponding to a shift between what appear to be two distinct operation modes (i.e. regimes A/B and regime D), as shown in Fig. 5. In the first mode, both datasets (I_d and I_e) show a narrowing of the breathing mode frequency band around 280 V. In the second mode, the amplitude of the breathing mode increases, appearing as two distinct frequencies at 20 and 30 kHz (see Fig. 7a) with a slightly higher amplitude at 30 kHz, as previously observed in the electron current study shown in Fig. 5b. Additionally, there is a noticeable gain in amplitude within the ITT frequency range. An analysis of the electron current corroborates these findings, and reveals a stable oscillation at 48 kHz within the discharge voltage range of 250 – 430 V (see Fig. 7b).

The study conducted on krypton revealed trends similar to those observed with xenon. Spectra reveal the presence of the breathing mode at approximately 8 kHz. As the discharge voltage increases, the frequency of this mode gradually

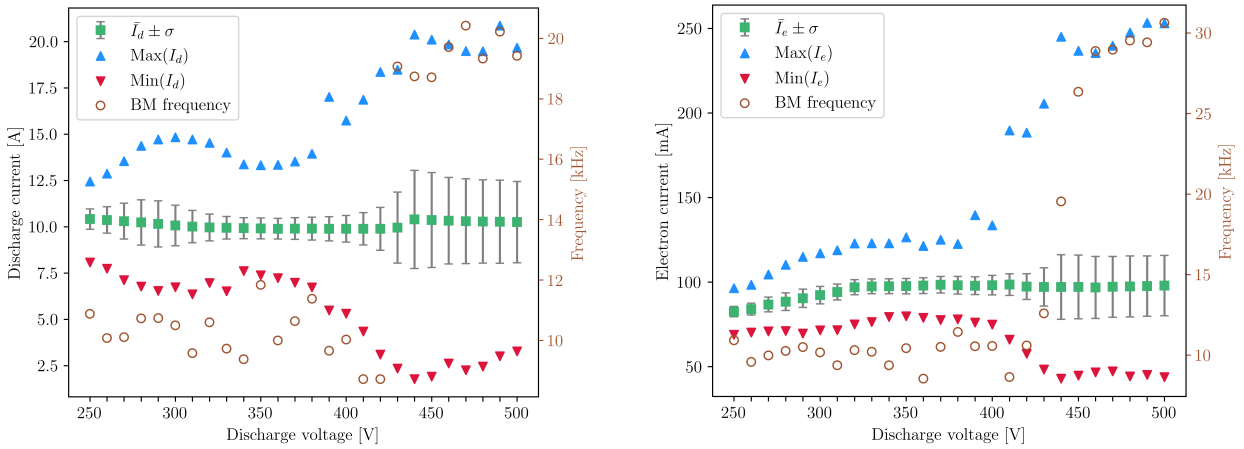

(a) Discharge current caracteristics with xenon.

(b) Electron current caracteristics with xenon.

Fig. 5 Thruster discharge current (a) and electron current (b) characteristics for 10.0 mg/s of xenon as a function of the discharge voltage. Brown circles indicate the breathing mode frequency, blue triangles represent the current maxima, red triangles correspond to the minima, and green squares denote the mean current value with associated standard deviation (error bars).

rises (in contrast to xenon, where a sharper transition is observed around 430 V), reaching 15 kHz. In terms of amplitude, a slight decline is observed within the discharge voltage range of 270 – 330 V. Additionally, a second frequency range of oscillations, spanning 18 – 55 kHz, is evident and persists across the entire study (see Fig. 8a). This range remains distinctly separate from the breathing mode up to 390 V, beyond which the two merge. Above 55 kHz, a reduction in amplitude is observed, extending through the range of 60 – 350 kHz. However, within this range — where ITT oscillations are typically observed — the amplitude increases with rising discharge voltage. Beyond the megahertz range, no oscillations are detected. This trend is mirrored in the electron current (see Fig. 8b), particularly in the evolution of the breathing mode. Furthermore, as the discharge voltage increases to 360 – 500 V, a second frequency range within the ITT domain emerges. Notably, a stable oscillation at 80 kHz is observed between 330 V and 450 V (see Fig. 8b), persisting throughout this voltage range.

2. As a function of the gas flow rate

A second study was conducted to investigate the effect of gas flow rate on plasma oscillations in Hall thrusters. For each gas, three discharge voltages were tested across varying flow rates (see Table 2). Figure 9 presents the two-dimensional contour plots obtained for xenon. The graphs corresponding to I_d are shown on the right side of the figure, while those for I_e are displayed on the left. The graphs are arranged in ascending order of discharge voltage, with 300 V, 400 V, and 450 V from top to bottom, respectively.

The dominant instability observed in Hall thrusters, as depicted in Fig. 9a, 9c and 9e, is the breathing mode. This finding is further corroborated by Fig. 9b, 9d and 9f. It can be seen that the frequency of the breathing mode remains unaffected by variations in the flow rate. However, the amplitude of this mode appears sensitive to changes in the flow rate, increasing as the flow rate rises. Notably, certain high flow rates exert a more pronounced effect on the breathing mode, as illustrated in Fig. 9a and Fig. 9b between 9 and 10 mg/s. This trend is also evident in Fig. 9c and Fig. 9d, with flow rates between 8 and 9 mg/s, and 11 and 12 mg/s. Figures 9e and 9f show the bifurcation of the breathing mode into two closely spaced modes at flow rates exceeding 10 mg/s. A closer examination of Fig. 9b, 9d and 9f reveals the presence of oscillations within the ITT range, spanning from 60 kHz to 250 kHz. These oscillations correlate with the observed amplitude variations of the breathing mode. Additionally, the graphs indicate an oscillation between 48 and 55 kHz, which is persistent in Fig. 9b and partial in Fig. 9d and 9f. The frequency of this oscillation appears to coincide with the fictitious line at which a significant decline in amplitude is observed in the I_d spectra. In conclusion, for each discharge voltage, there exists a specific flow condition where the breathing mode is most dominant.

Figure 10 presents the two-dimensional contours obtained with krypton for identical discharge voltages. The only variable that has been altered is the flow rate, adjusted to ensure it does not exceed the high-power range of the thruster.

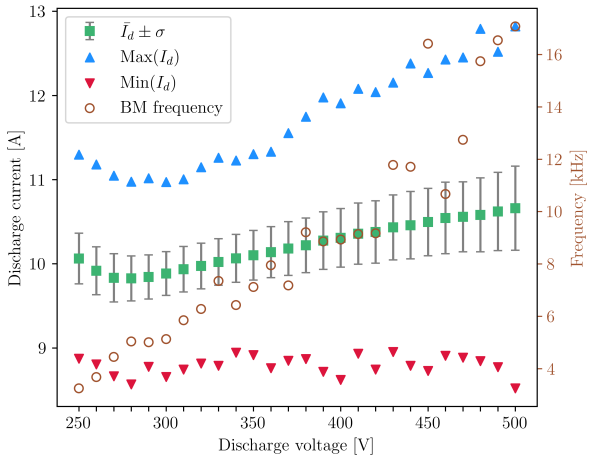

(a) Discharge current caracteristics with krypton.

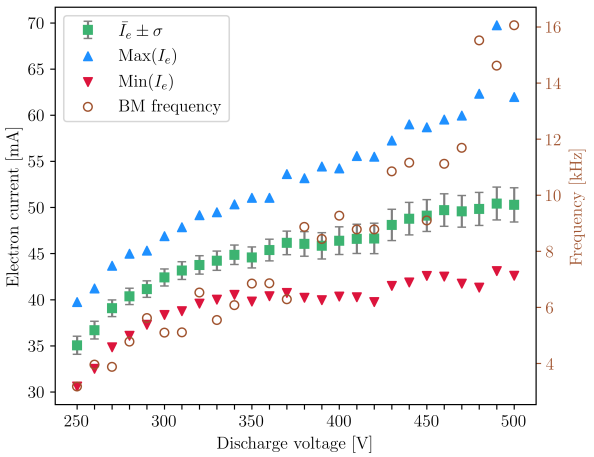

(b) Electron current caracteristics with krypton.

Fig. 6 Thruster discharge current (a) and electron current (b) characteristics for 8.0 mg/s of krypton as a function of the discharge voltage. Brown circles indicate the breathing mode frequency, blue triangles represent the current maxima, red triangles correspond to the minima, and green squares denote the mean current value with associated standard deviation (error bars).

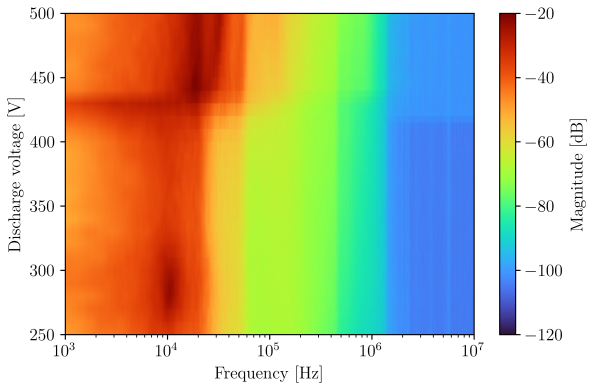

(a) Discharge current oscillations with respect to the discharge voltage.

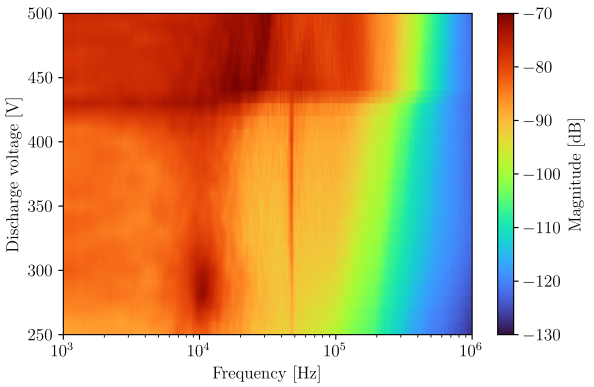

(b) Electron current oscillations with respect to the discharge voltage.

Fig. 7 2D spectrograms of oscillations in the discharge current (a) and electron current (b) of the thruster operating with xenon. Time-series were recorded at 10 V increments.

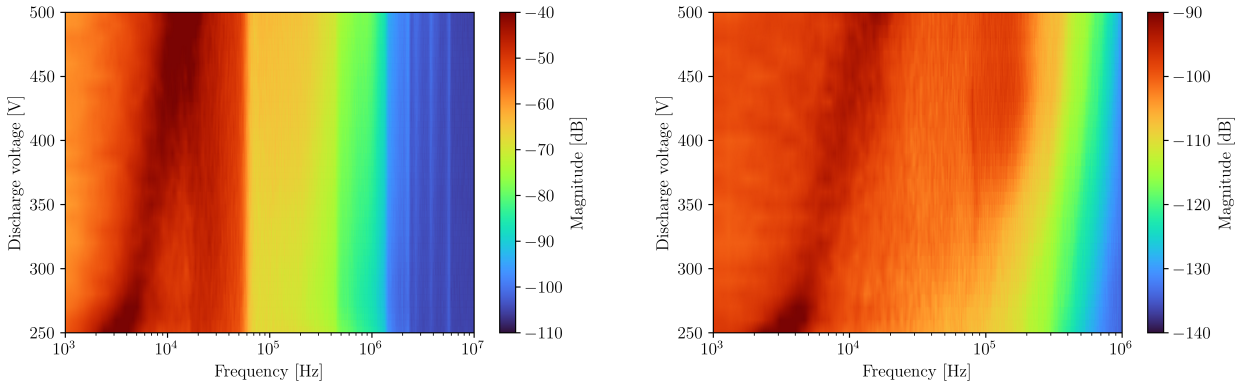

(a) Discharge current oscillations with respect to the discharge voltage.

(b) Electron current oscillations with respect to the discharge voltage.

Fig. 8 2D spectrograms of oscillations in the discharge current (a) and electron current (b) of the thruster operating with krypton. Time-series were recorded at 10 V increments.

All figures confirm the presence of the breathing mode throughout the study. However, in contrast to the xenon results, the frequency of the breathing mode increases with flow rate. Its amplitude also rises with increasing flow rate, but this effect is observed only for discharge voltages of 400 V and 450 V. The same trend is noted for oscillations within the ITT range [80 - 200 kHz]. At 300 V, we also observed a second mode within the 17 - 55 kHz range, which narrows to approximately 17 kHz as the flow rate increases. Aside from the frequency shift of the breathing mode, the overall behavior is similar to that observed with xenon.

B. Electron and discharge currents time-frequency domain analysis for both xenon and krypton

1. Time-series selected to apply WT and HHT

Figure 11 illustrates the time-series segments for the various xenon operating points (for further details, refer to Table 3), each of which will be subjected to a wavelet transform. In each subfigure, the discharge current (I_d) is represented in blue, while the electron current (I_e) is shown in green. These values were recorded simultaneously. The flow rate remains constant across all operating points, with only the discharge voltage varying. In general, the discharge current shows an increase in oscillation amplitude as the voltage rises. Additionally, the breathing mode is clearly identifiable, particularly on the I_d trace. A comparison of the two currents reveals that, in addition to the breathing mode, the electron current exhibits a higher-frequency component, approximately 100 kHz, consistent with earlier observations in the two-dimensional spectra. The sub-figures can be divided into two distinct categories: the top range (280–360 V), where oscillation amplitudes are relatively small, and the bottom range (430–500 V), where they are significantly larger. Sub-figures 4 and 5 are of particular interest, standing out due to their distinctive characteristics. For OP4 (i.e. sub-figure 4), the time segment reveals intermittent behavior, with alternating periods of low oscillations (approximately 500 μs) and high oscillations (approximately 800 μs). In OP5, a narrow peak (5 – 10 μs) in the electron current is observed regularly, with fluctuations of approximately 80 mA. These events predominantly occur during the decay phase of the discharge current. A similar peak is observed in OP6, also occurring during the decay phase.

Figure 12 illustrates the time-series segments for the various krypton operating points (for further details, refer to Table 4), which will be subjected to a wavelet transform. The discharge current is depicted in violet, while the electron current is represented in pink. Unlike the previous figure, the gas flow is not constant in this case. Operating points OP4 and OP6 were specifically selected for their differing discharge behaviors. The remaining operating points (OP1, OP2, OP3, and OP5) exhibit identical flow rates, with only voltage variation. The breathing mode is observable in the krypton series; however, this is not the case for the electron current, except in OP6. In addition to the primary breathing mode component, a secondary component with a frequency of approximately 100 kHz (ITTs) is superimposed on both I_d and I_e.

Figure 11 and Fig. 12 reveal that only one operating point, OP5 for xenon and OP4 for krypton, exhibits similar temporal behavior in both the discharge current (characterized by a clear breathing mode) and the electron current (marked by narrow peaks in the decay phase of I_d). In this operating configuration, the propellant is the only variable,

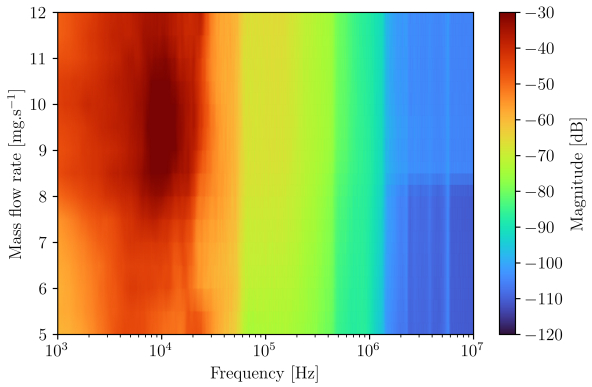

(a) Discharge current oscillations at 300 V.

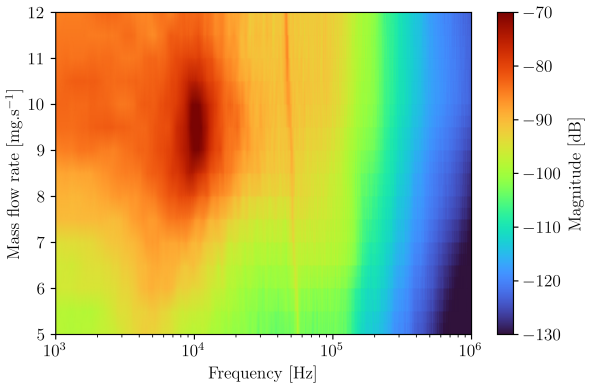

(b) Electron current oscillations at 300 V.

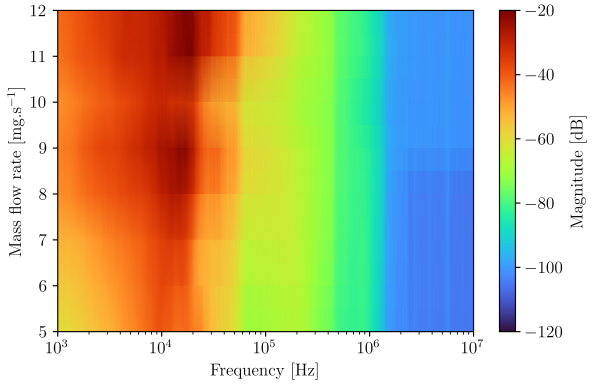

(c) Discharge current oscillations at 400 V.

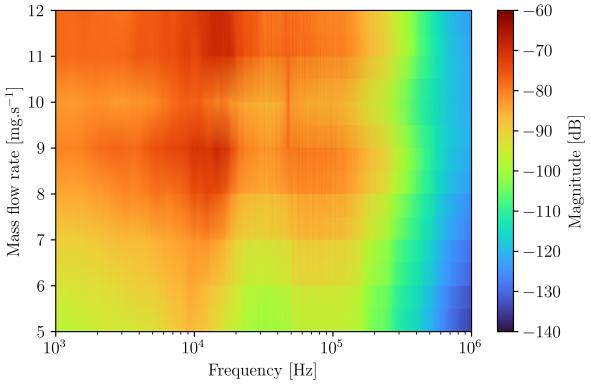

(d) Electron current oscillations at 400 V.

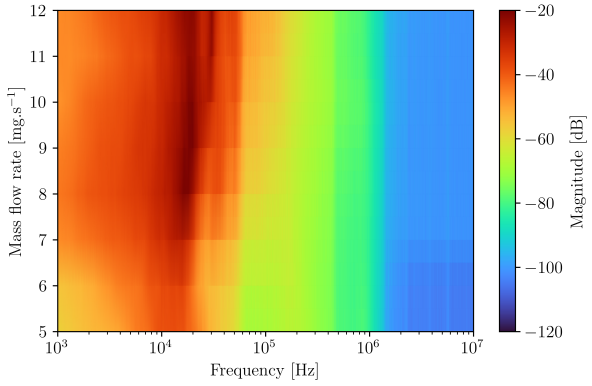

(e) Discharge current oscillations at 450 V.

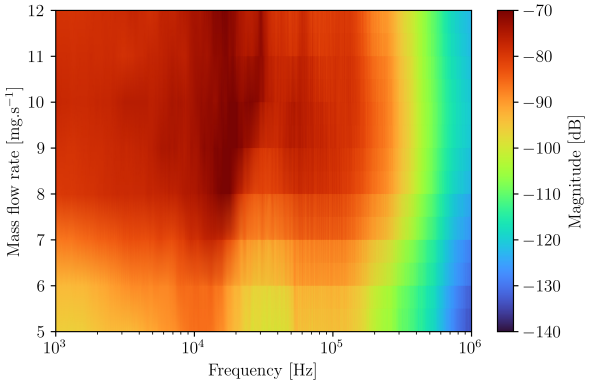

(f) Electron current oscillations at 450 V.

Fig. 9 2D spectrograms of broadband oscillations in the discharge current (a, c, e) and electron current (b, d, f) of the thruster operating with xenon at 300 V, 400 V and 450 V, respectively. Time-series were recorded at 0.5 mg/s increments in flow rate.

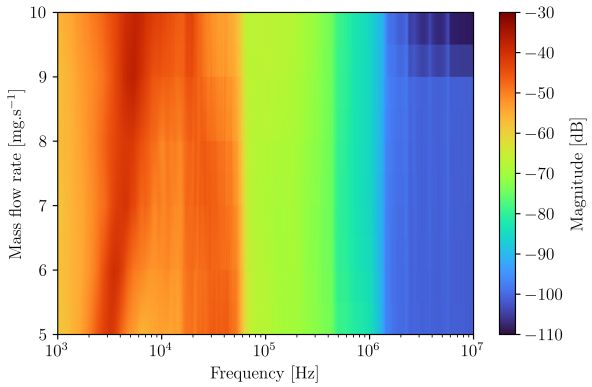

(a) Dischare current oscillations at 300 V.

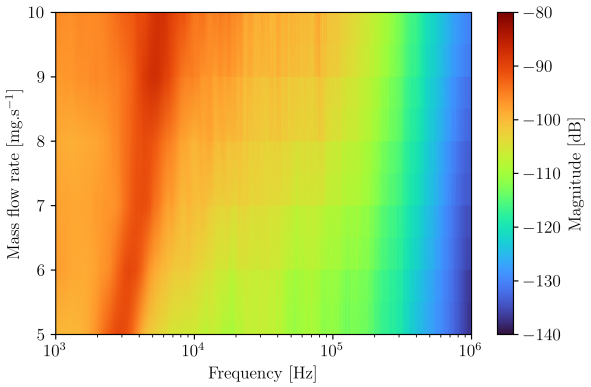

(b) Electron current oscillations at 300 V.

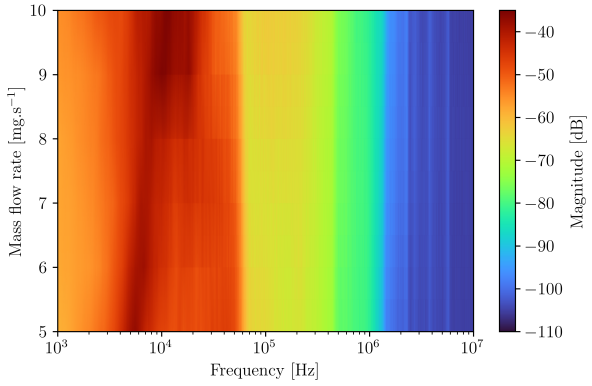

(c) Dischare current oscillations at 400 V.

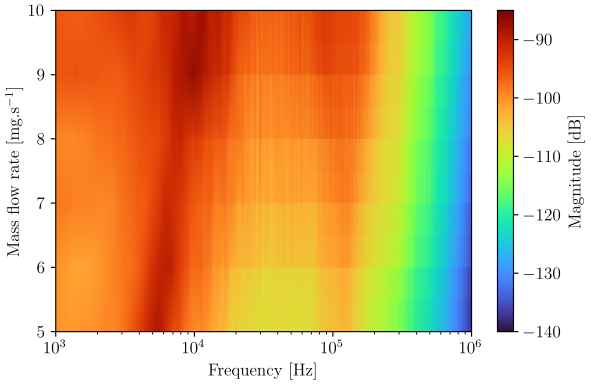

(d) Electron current oscillations at 400 V.

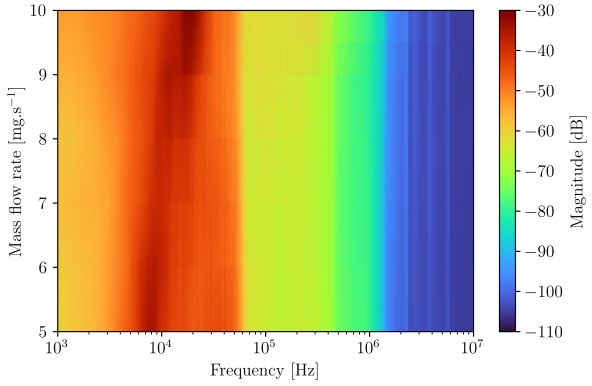

(e) Dischare current oscillations at 450 V.

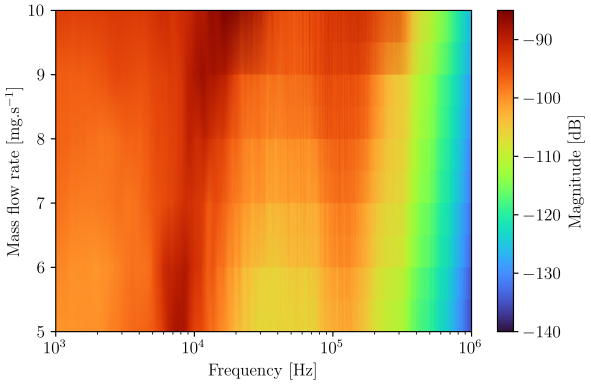

(f) Electron current oscillations at 450 V.

Fig. 10 2D spectrograms of broadband oscillations in the discharge current (a, c, e) and electron current (b, d, f) of the thruster operating with krypton at 300 V, 400 V and 450 V, respectively. Time-series were recorded at 1.0 mg/s increments in flow rate.

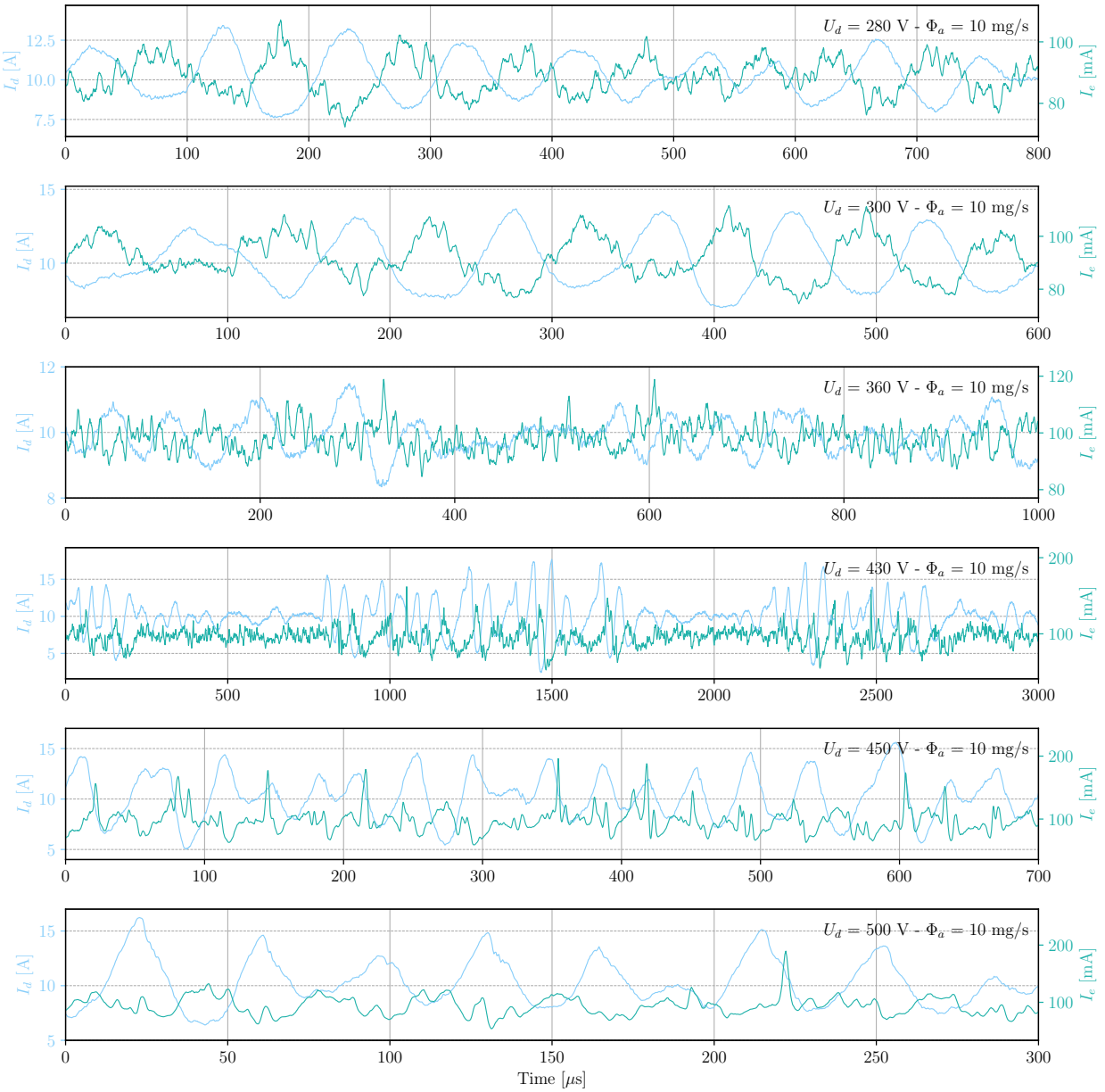

Fig. 11 Time-series employed for wavelet transform (WT) during thruster operation with xenon, showing discharge current (light blue) and electron current (green). Operating conditions are indicated in the top-left corner of each subplot.

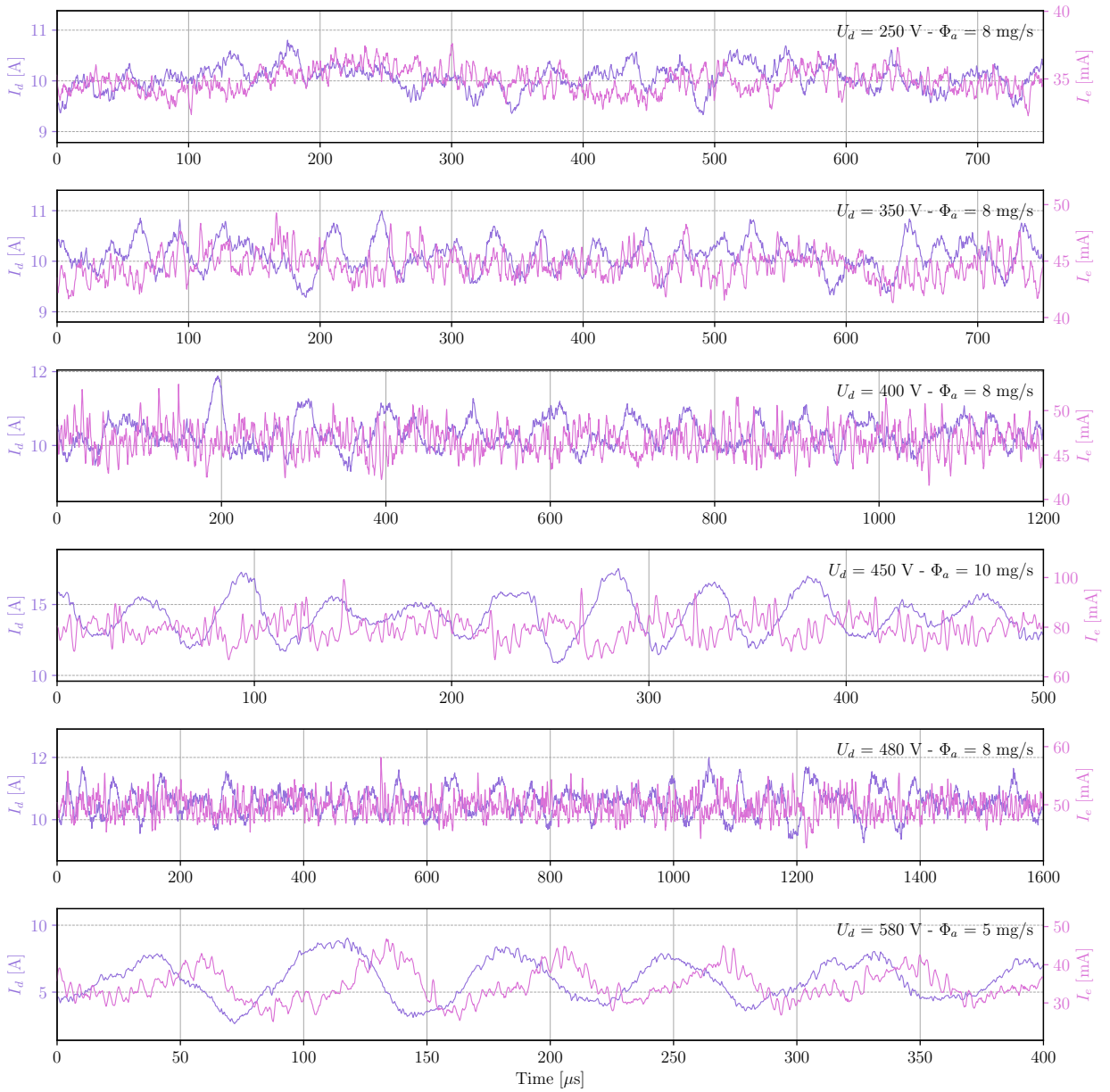

Fig. 12 Time-series employed for wavelet transform (WT) during thruster operation with krypton, showing discharge current (purple) and electron current (pink). Operating conditions are indicated in the top-left corner of each subplot.

while the discharge voltage and gas flow remain identical.

2. Wavelet transform analysis when the thruster fires with xenon

The Morlet wavelet, with parameters (β_b = 4, f_0 = 1), was selected as the mother wavelet for the wavelet transform analysis.

Discharge current time-series

Figure 13 illustrates the application of the wavelet transform to the discharge currents measured for xenon. Compared to the Fourier transform analysis on the left of each spectrogram, the wavelet transform exhibits no discontinuity over the breathing mode range. However, a reduction in mode intensity is evident in Fig. 13d, which corresponds to the observed intermittency. Additionally, Fig. 13a, 13b, and 13c reveal the presence of relatively persistent oscillations within the 50 – 400 kHz range. No discernible permanent or non-permanent frequencies are observed outside this range. As shown in Fig. 13d, the intermittency identified in the time-series (Fig. 11) is once again apparent on the spectrogram. The breathing mode becomes more pronounced and spans a broader frequency range during periods of strong oscillation. During these phases, additional frequencies temporarily emerge in the 60 – 200 / 300 kHz range, persisting for brief durations (50 – 100 μs). This phenomenon appears to coincide with the decay phase of the discharge current, where the slope is particularly steep. Moreover, the intensity of the signal increases as it crosses the mean value and approaches a local minimum, as indicated by the dotted lines. Figures 13e and 13f demonstrate a high degree of similarity. Both reveal a stable breathing mode over time, which becomes tighter as the signal adopts a sawtooth-like shape and less so as the signal transitions toward a sinusoidal form. The spectrogram corroborates the existence of a persistent oscillation at approximately 50 kHz, consistent with the Fourier spectrum result. Additionally, both spectrograms display oscillations within the 70 kHz to 1 MHz range. The Fourier transform further confirms oscillations in the 100 – 400 kHz range, with peak intensity at 150 kHz in Fig. 13e and within the 80 – 450 kHz range with peak intensity at 120 kHz in Fig. 13f. This range can be attributed to ion transit-time (ITT) oscillations. Another notable observation is the extension of these oscillations toward 1 MHz, which is most prominent in the spectrogram of Fig. 13f. This region is particularly associated with electron dynamics. A comparison of the time-series and the spectrogram reveals that the emergence of this frequency coincides with the initial descent of the signal (time-segment of Fig. 13f), especially during phases where the signal assumes a plateau-like shape (refer to dotted lines). In conclusion, this study demonstrates that the presence of ion transit-time (ITT) oscillations becomes increasingly evident as the discharge voltage rises. This is reflected in the time-series as an increase in oscillation amplitude, accompanied by either sinusoidal (Fig. 13d) or sawtooth-shaped (Fig. 13f) behavior. Additionally, oscillations at frequencies near 1 MHz have been observed, correlating with specific signal morphologies. Notably, these phenomena occur exclusively when ITTs are present during specific time intervals, reminiscent of the narrowing of a flame at its extremity (indicated by the dotted line in Fig. 13f).

Electron current time-series

The spectrograms obtained from the wavelet transform of the electron current further substantiate the previously discussed observations. First and foremost, each of the aforementioned spectrograms corroborates the continuity of the breathing mode over time. As shown in Fig. 14a, 14b, and 14c, oscillations within the ITT range are consistently present across the analyzed signal. However, Fig. 14a highlights a pronounced intensification of these oscillations during the decay phase of the signal (see dotted lines). Figure 14d reaffirms the intermittency phenomenon previously examined. It reveals that the intensity of frequencies within the ITT range is locally enhanced during periods of significant oscillation. Additionally, Fig. 14e and 14f confirm the existence of transient oscillations — clearly identifiable as "flames" — within the ITT range. The regions labeled as "flames" in Fig. 14e correspond to peaks in the analyzed signal, as indicated by the dotted lines. Consistent with earlier observations, these peaks (Fig. 14e) predominantly occur during the decay phase of the discharge current (Fig. 13e), demonstrating a strong positive correlation between the two currents (I_d and I_e - Fig. 11, sub-figure 5). In the case of Fig. 14f, the spectrogram showcases a series of flames corresponding to those observed in Fig. 13f (via the transform). One particular flame, highlighted by the dotted line (Fig. 14f), aligns with the sole peak in the signal (I_e) under consideration. The emergence of this peak is also correlated with the decay phase of the discharge current, as depicted in Fig. 11 (sub-figure 6). This region is also part of the time segment containing a component at approximately 1 MHz. Figure 14f thus confirms the presence of highly localized oscillations around 1 MHz.

3. Wavelet transform analysis when the thruster fires with krypton

The time-frequency analyses performed during the operation of the thruster with krypton are presented in Fig. 15 for the discharge current and Fig. 16 for the electron current. It is important to note that the operating points OP1, OP2,

OP3, and OP5, depicted in Fig. 15a, 15b, 15c, 15e, and 16a, 16b, 16c, 16e, respectively I_d and I_e, are characterized by identical gas flow rates but differ in discharge voltages.

Discharge current time-series

An initial analysis of the discharge current reveals the presence of a persistent breathing mode, as evidenced by the consistency of the trends observed across all graphs. As shown in Fig. 15a, 15b and 15c, the breathing mode occurs at frequencies below 10 kHz. A broader frequency range, between 15 and 60 kHz, is also detected, albeit with lower intensity, as corroborated by the Fourier spectrum shown on the left of each graph. Figure 15e indicates that higher discharge voltages correspond to an elevated frequency range for the breathing mode. Consequently, the two lower-frequency ranges observed in Fig. 15a, 15b and 15c are merged, forming a unified range that extends up to 60 kHz. Oscillations between 100 and 500 kHz are also observed to persist throughout the analysis. Figures 15d and 15f further illustrate the presence of a secondary, persistent frequency band following the breathing mode, spanning from 30 to 60 kHz. However, the width of this band fluctuates over time. Notably, Fig. 15d and 15f provide significant insights into the ITT range (100 - 500 kHz). Unlike the other figures, these oscillations are not continuous but instead occur at specific, well-defined moments in time, coinciding with the decline in the discharge current. In Fig. 15d, a plateau-like shape is observed (see dotted lines), which mirrors the behavior noted in the xenon time-series. In contrast, Fig. 15f shows that these oscillations, in the 200 - 400 kHz range, are associated with an increase in amplitude (see dotted line), relative to the main breathing mode component.

Electron current time-series

Figure 16 illustrates the spectrograms corresponding to the wavelet transform of the electron currents during thruster operation with krypton. These figures collectively confirm the continuity of the breathing mode (BM) without any discrepancies. In Fig. 16a, 16b, 16c, and 16e, no discernible trends or singular events are observed, and the oscillations within the ITT range appear to remain constant over time. Figure 16d, however, reveals oscillations within the 100 - 500 kHz range, as confirmed by the Fourier spectrum. These oscillations are more persistent and exhibit a characteristic "flame" shape, which is evident during brief moments (see dotted lines), corresponding to the peaks observed in the time-domain signal. In Fig. 16f, the second low-frequency mode becomes apparent in the wavelet transform. Notably, the oscillations in the ITT range appear to be highly localized (1 - 2 events) during the same time segment under study in Fig. 15f (see dotted lines). In conclusion the investigation also revealed the occurrence of transient oscillations within the ITT range when operating with krypton. These oscillations were found to correlate with the decay phase of the breathing mode oscillations in the discharge current. Additionally, when these oscillations appear in the discharge current spectrograms, they are also discernible in the corresponding electron current spectrograms, where they manifest as steep slopes.

Conclusion

The current analysis of the thruster operating with xenon demonstrates that ITT oscillations are not a persistent phenomenon. A clear correlation between the discharge current (I_d) and the electron current (I_e) was successfully established. Indeed, the electron current exhibited a 150 ° - 180 ° phase shift relative to the discharge current, if we consider the main oscillation (i.e. the breathing mode). Moreover, a strong correlation was observed during ITT oscillations, especially when these oscillations were pronounced, with the electron current showing significant amplitude variations at local peaks. For krypton, a similar correlation between the discharge current and the electron current was evident, both at the phase shift level and within the primary oscillation regime. For both propellants, the electron current proved to be a more sensitive indicator of oscillations within the ITT range, providing valuable insights into the dynamics of the thruster operation.

4. Huang-Hilbert transform analysis when the thruster fires with xenon

In this section, a study interval of 1 millisecond was selected for the EMD technique, while a 2-millisecond interval was employed for the marginal spectrum. It is important to note that the time-series segment chosen for this study differs from the one used in the wavelet transform analysis. This distinction facilitates an evaluation of whether the events under investigation are inherent to the signal or transient in nature.

In accordance with the wavelet transform study, the OP4 operating point with xenon (see Table 3 and Fig. 11) was selected for the application of the HHT. Figure 17a depicts the initial step of the transform, which involves decomposition into n^{th} Intrinsic Mode Functions (IMFs) using the EMD technique. The last two traces at the bottom of the figure represent the global residual and the reconstructed signal, respectively. Figure 18a presents the second step of the transform, the marginal spectrum, obtained by integrating the Hilbert spectra of all IMFs.

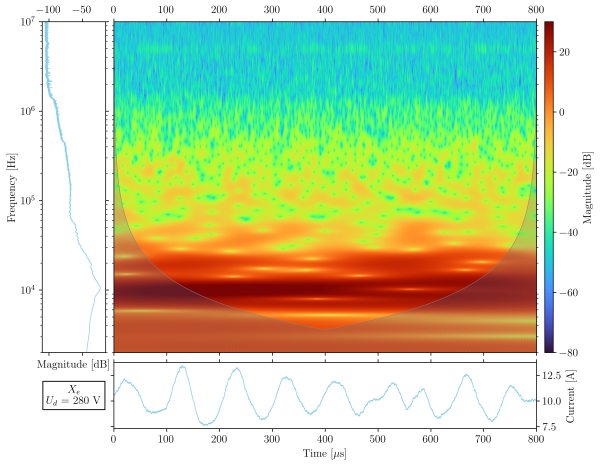

(a) Regime A

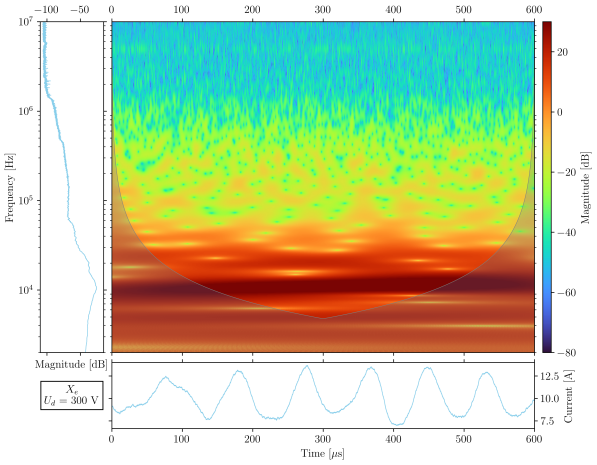

(b) Regime A

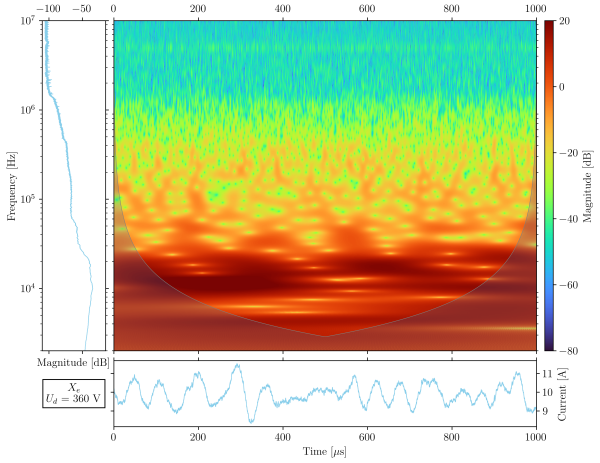

(c) Regime B

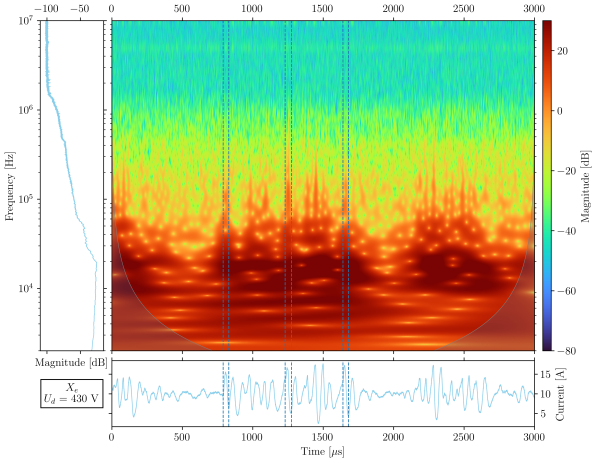

(d) Regime C

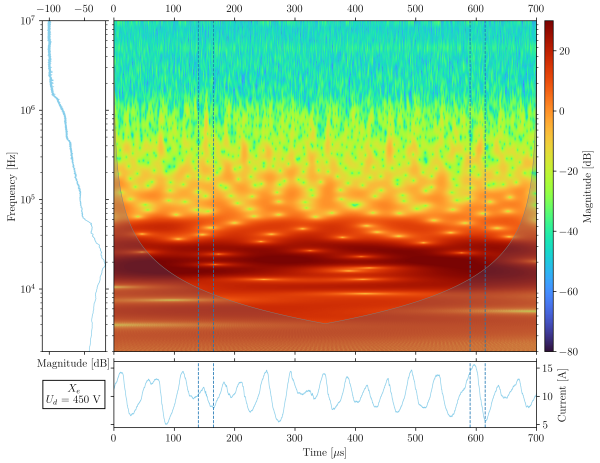

(e) Regime D

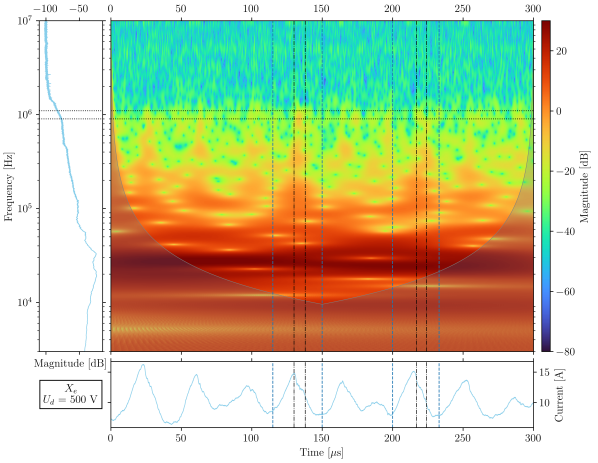

(f) Regime D

Fig. 13 Wavelet spectrograms of the discharge current for each selected operating point with xenon. The main figure depicts the spectrogram of the chosen time segment, which is displayed as the bottom curve. The x-axis represents time, the y-axis represents frequency, and the color bar (logarithmic scale) indicates the Power Spectral Density. The shaded region represents the cone of influence, marking the area where the coherence of the wavelet transform may be reduced due to edge effects. The graph on the left shows the Fourier spectrum of the entire time series.

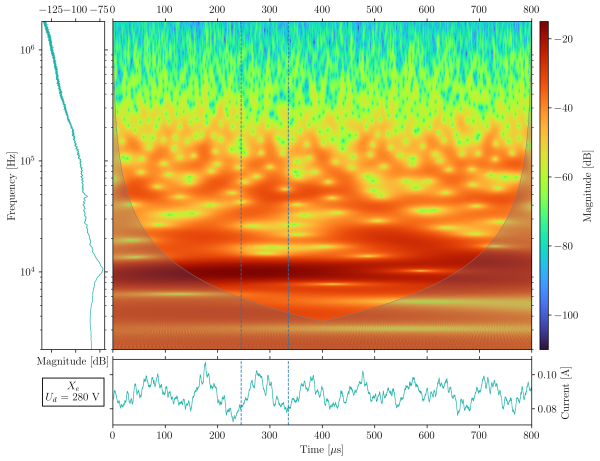

(a) Regime A

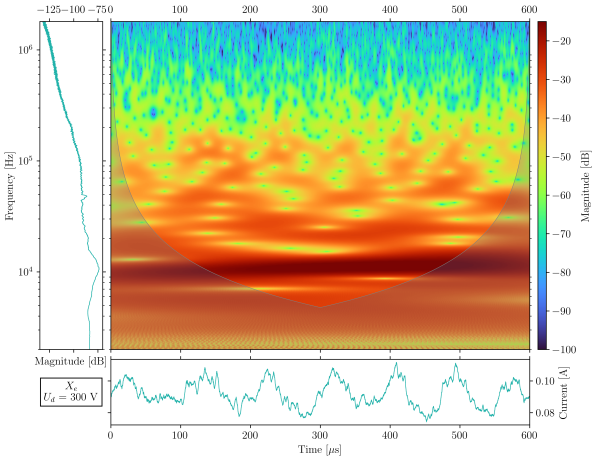

(b) Regime A

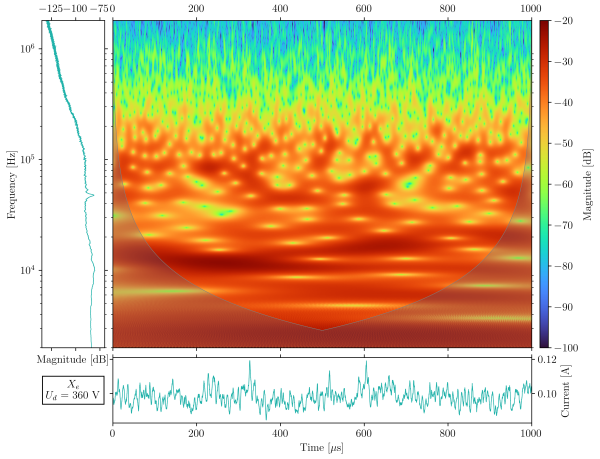

(c) Regime B

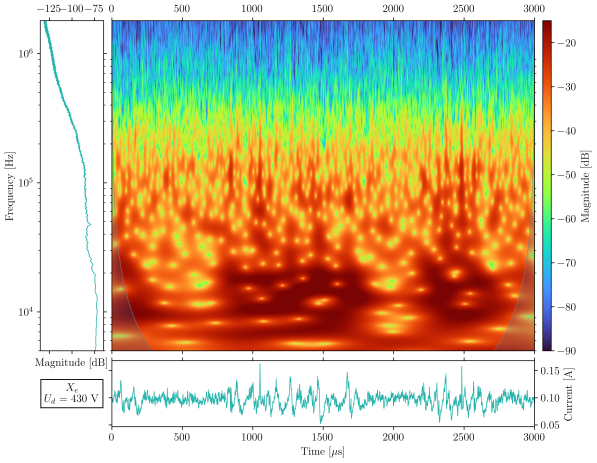

(d) Regime C

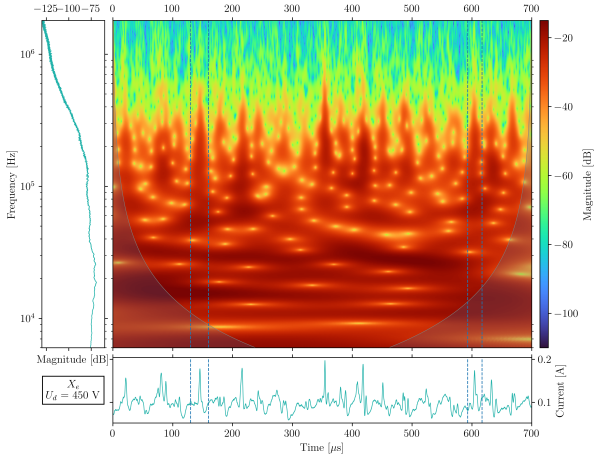

(e) Regime D

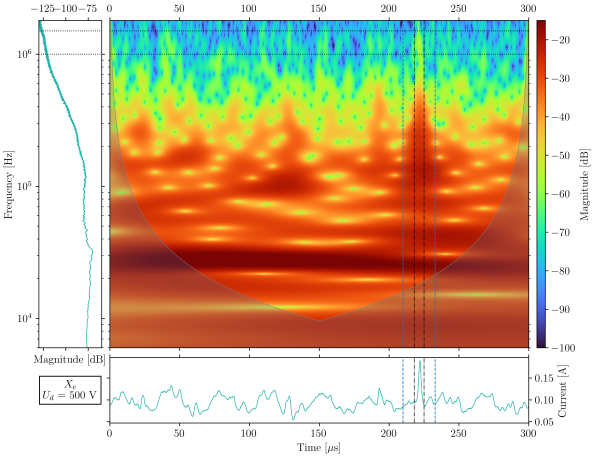

(f) Regime D

Fig. 14 Wavelet spectrograms of the electron current for each selected operating point with xenon. The main figure depicts the spectrogram of the chosen time segment, which is displayed as the bottom curve. The x-axis represents time, the y-axis represents frequency, and the color bar (logarithmic scale) indicates the Power Spectral Density. The shaded region represents the cone of influence, marking the area where the coherence of the wavelet transform may be reduced due to edge effects. The graph on the left shows the Fourier spectrum of the entire time series.

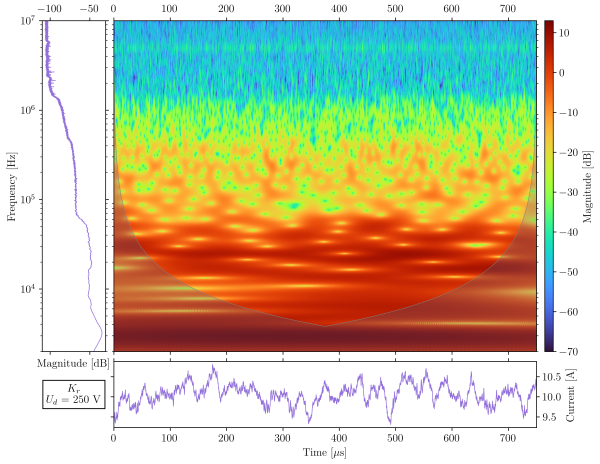

(a) Regime A

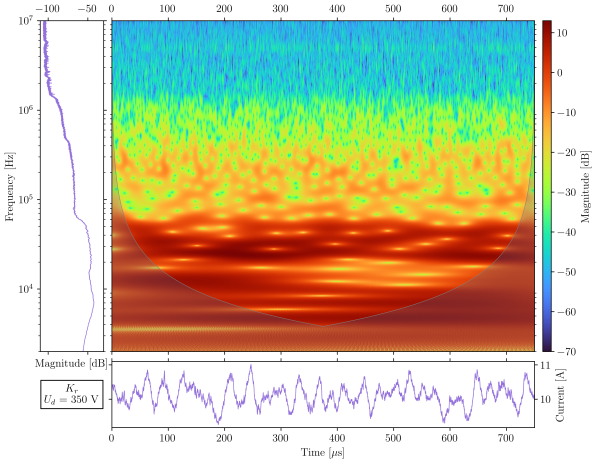

(b) Regime B

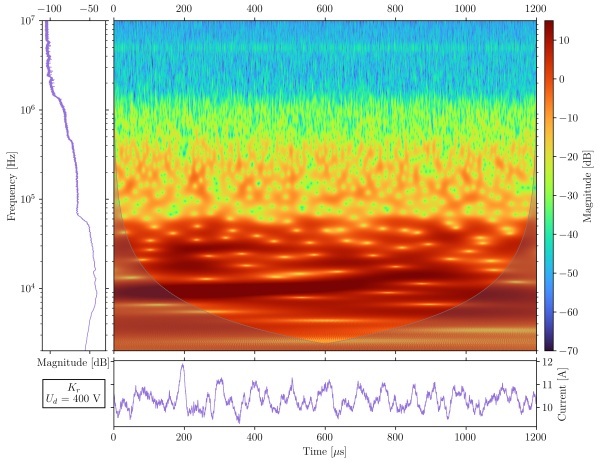

(c) Regime B

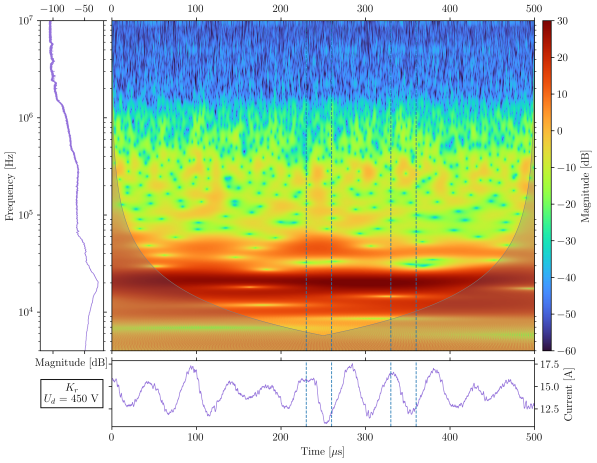

(d) -

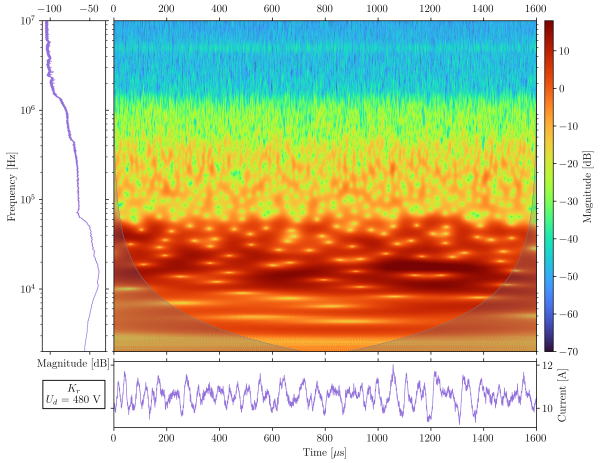

(e) Regime B

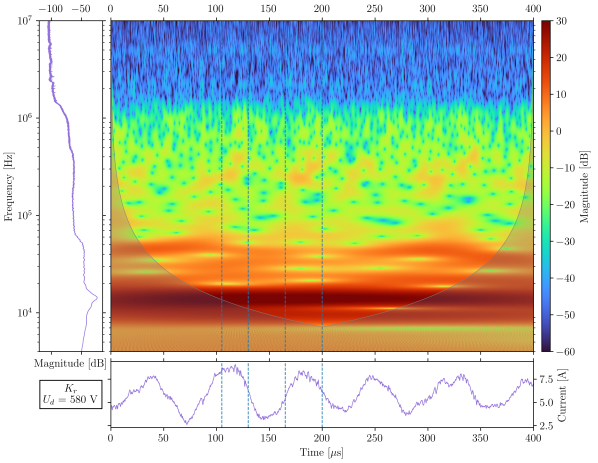

(f) -

Fig. 15 Wavelet spectrograms of the discharge current for each selected operating point with krypton. The main figure depicts the spectrogram of the chosen time segment, which is displayed as the bottom curve. The x-axis represents time, the y-axis represents frequency, and the color bar (logarithmic scale) indicates the Power Spectral Density. The shaded region represents the cone of influence, marking the area where the coherence of the wavelet transform may be reduced due to edge effects. The graph on the left shows the Fourier spectrum of the entire time series.

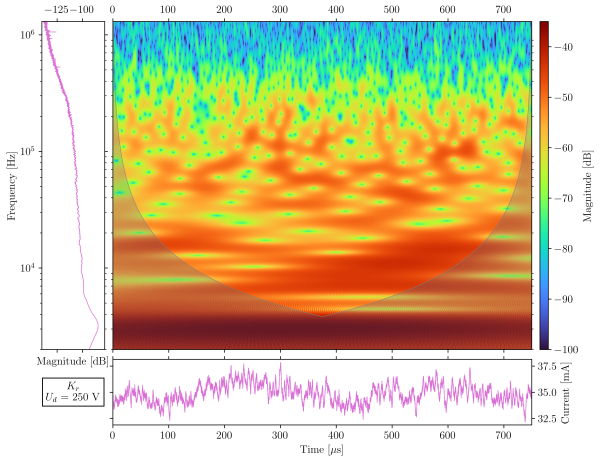

(a) Regime A

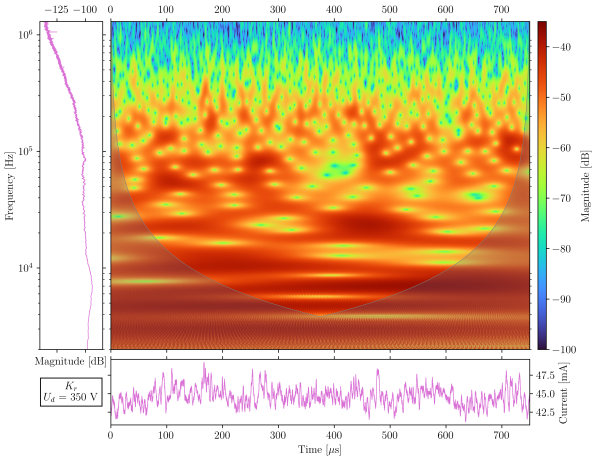

(b) Regime B

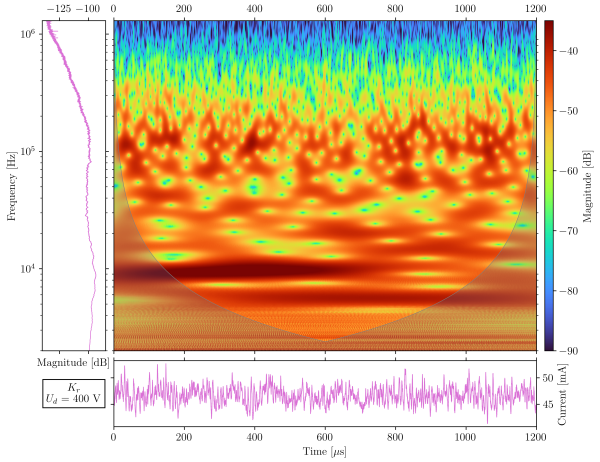

(c) Regime B

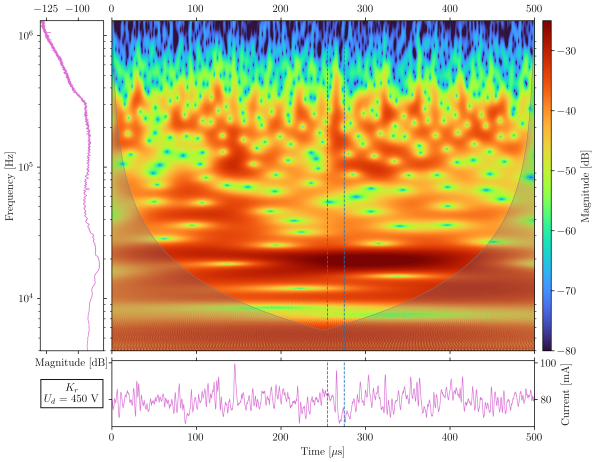

(d) -

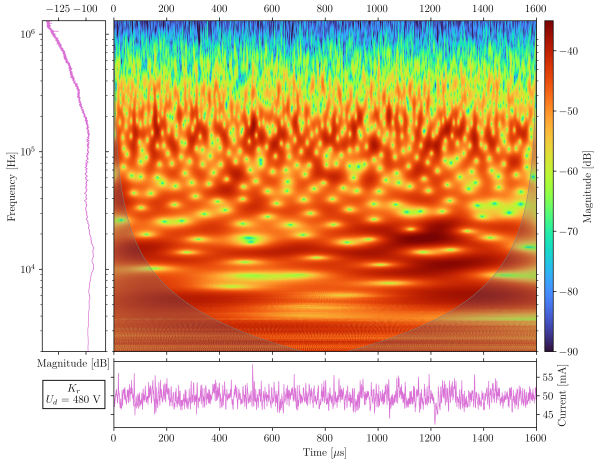

(e) Regime B

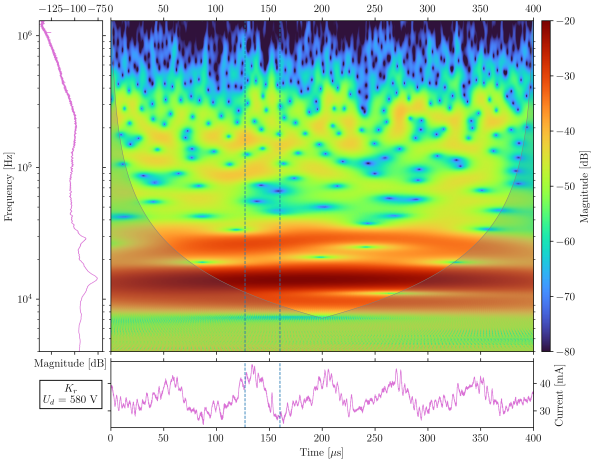

(f) -

Fig. 16 Wavelet spectrograms of the electron current for each selected operating point with krypton. The main figure depicts the spectrogram of the chosen time segment, which is displayed as the bottom curve. The x-axis represents time, the y-axis represents frequency, and the color bar (logarithmic scale) indicates the Power Spectral Density. The shaded region represents the cone of influence, marking the area where the coherence of the wavelet transform may be reduced due to edge effects. The graph on the left shows the Fourier spectrum of the entire time series.

Table 5 Mean frequencies of the Intrinsic Mode Functions for OP4 with xenon.

IMFs N°	Mean frequency kHz	Type of oscillations -
1	1,200	-
2	534	ITT
3	219	ITT
4	48.6	BM
5	18.2	BM
6	7.9	BM
7	4	-
8	2.1	-

As the name indicates, the EMD technique requires a user-defined input parameter: the number of modes (n) desired in the decomposition. Based on previous studies of similar signals [34] and the outcomes of preliminary iterations, eight modes were determined to be optimal. The frequencies associated with each mode are listed in Table 5. The intrinsic mode functions are numbered from 1 to 8 in descending order of frequency, spanning a range from MHz to kHz. The first mode, with a mean frequency of 1.2 MHz, corresponds to residual noise without specific features. IMFs 2 and 3 exhibit distinct frequencies of 534 kHz and 219 kHz, respectively. While the overall amplitudes of these two modes are similar, local amplitude peaks are more pronounced in IMF 3 (e.g., a peak-to-peak amplitude of 1 A at t = 0.8 ms). These modes are identified as ITT oscillations.

Modes 4, 5, and 6 correspond to mean frequencies of 48.6 kHz, 18.2 kHz, and 7.9 kHz, respectively. Given that the breathing mode typically lies within the 10–50 kHz range, modes 4 and 5 can be considered representative of this common Hall thruster oscillation. Mode 6, while slightly outside the lower limit of the breathing mode range, also aligns with this behavior. Modes 7 and 8, with (low) frequencies of 4 kHz and 2.1 kHz, respectively, fall outside the established ranges for Hall thruster instabilities. A detailed analysis of these modes will not be further pursued in this study.

A strong correlation between ITT and breathing mode oscillations is particularly evident when analyzing the four primary IMFs (2, 3, 4, and 5). Major peaks are distinctly identifiable at 0.45 ms and 0.8 – 0.85 ms in IMFs 2 and 3. Corresponding oscillations in the breathing mode are observed for the same time intervals in IMFs 4 and 5. A closer examination of the IMF 4 signal reveals two distinct waveforms: a sinusoidal wave at 0.45 ms and a sawtooth wave at 0.83 ms, both of which are mirrored in the ITT modes, i.e. IMFs 2 and 3. In addition, the signal in IMF 4 is highly intermittent with 0.25 ms of oscillations observed over a 1-ms interval. Notably, a high-amplitude signal with a plateau during the decay phase (IMF 5 at t = 0.81 ms) appears to be mirrored exclusively in IMF 3. This indicates that the waveform and amplitude of the BM oscillation infiuence the ITTs. Additionally, an oscillation at approximately 50 kHz (IMF 4) impacts both ITT modes, while a second oscillation at approximately 18 kHz (IMF 3) is reflected only in one ITT mode (IMF 3 - 219 kHz).

The findings of this Huang-Hilbert transform study further substantiate the conclusions drawn from the earlier wavelet transform analysis. Specifically, it is confirmed that certain signal shapes and amplitudes enhance the prominence of ITTs, although their presence is not strictly dependent on these conditions.

The marginal spectrum, derived over a 2 ms interval, provides additional evidence for the presence of IMF 3 associated with the BM and IMF 4 corresponding to ITT oscillations within the broad 100 – 250 kHz frequency range. This result aligns closely with the observations made from the Fig. 13d analysis.

5. Huang-Hilbert transform analysis when the thruster fires with krypton

In this section, we performed the HHT under the same conditions as previously, i.e. 1 ms time segment for the EMD, input-parameter of eight modes, and a 2-ms interval for the marginal spectrum.

Consistent with the wavelet transform study, the OP4 operating point with krypton (see Table 4 and Fig. 12) was selected for the application of the HHT. Figure 17b illustrates the initial phase of the transform, which involves decomposition into 8 IMFs using the EMD technique. The last two traces at the bottom of the figure represent the global residual and the reconstructed signal, respectively. Figure 18b displays the last part of the transform, the marginal

Table 6 Mean frequencies of the IMFs for OP4 with krypton.

IMFs N°	Mean frequency kHz	Type of oscillations -
1	900	Electron dynamics
2	374	ITT
3	174	ITT
4	28.4	BM
5	14.9	BM
6	7.2	BM
7	3.9	-
8	1.8	-

spectrum, obtained by integrating the Hilbert spectra of all IMFs.

The frequency associated with each mode is summarized in Table 6, with modes numbered from 1 to 8 in descending order of mean frequency, ranging from MHz to kHz. Mode 1, characterized by a mean frequency of 0.9 MHz, exhibits features consistent with both the marginal spectrum and the spectrogram under investigation for this operating point, as shown in Fig. 18b and Fig. 15d, respectively. Modes 2 and 3 demonstrate distinct frequencies of 374 kHz and 174 kHz, respectively. Notably, the amplitude of the current in mode 2 exceeds that of mode 3, as evidenced by local extremums (e.g., a peak-to-peak amplitude of 0.9 A at t = 0.6 ms), compared to mode 3 with a maximum peak-to-peak amplitude of 0.4 A. These modes correspond to Ion Transit Time (ITT) oscillations and are therefore prominent on the marginal spectrum, as illustrated in Fig. 18b.

Modes 4, 5, and 6 with mean frequencies of 28.4 kHz, 14.9 kHz and 7.2 kHz, respectively, are also observed on the marginal spectrum in Fig. 18b. Modes 4 and 5 mean frequencies align with the typical range for the breathing mode, commonly identified between 10 and 50 kHz. Consequently, modes 4 and 5 are considered representative of this characteristic Hall thruster (HT) mode. Additionally, we can notice a stop in the BM oscillation for 0.1 ms in mode 4. Mode 6, while slightly outside the lower limit of the breathing mode range, also aligns with this behavior. Conversely, modes 7 and 8, with frequencies of 3.9 kHz and 1.8 kHz, respectively, lie outside the established frequency range for HT instabilities. As a result, further analysis of these modes is not provided.

A correlation becomes apparent when examining the four principal IMFs, specifically IMFs 2, 3, 4, and 5. This correlation is particularly notable between IMFs 3 (ITT) and 4 (BM). Notably, IMF 4 exhibits a discernible grouping of strong sinusoidal oscillations within the intervals of 0.25 – 0.35 ms and 0.8 – 1 ms. During these same time intervals, the oscillations observed in IMF 3 indicate improved periodicity and a more stable standard deviation. However, the oscillations present in IMF 4 do not appear to influence those in IMF 2. Similarly, IMF 5 displays no discernible correlation with the two modes associated with ITTs. The findings of this HHT analysis corroborate the conclusions drawn from the WT analysis (see V.B.3). Specifically, the results confirm that certain sinusoidal patterns with high amplitudes strongly favor the presence of ITTs. However, the presence of such patterns is not a strict requirement for ITT oscillations to manifest.

Conclusion

As demonstrated in the wavelet transform analysis, xenon and krypton significantly influence discharge behavior. For xenon, a persistent breathing mode (BM) with greater amplitudes is observed, alongside intermittent intervals where ITT oscillations become prominent. In contrast, krypton exhibits a continuous breathing mode coupled with permanent ITT oscillations with stronger amplitudes. For both gases, the EMD analysis identifies two modes associated with ITTs and three within the BM frequency range.

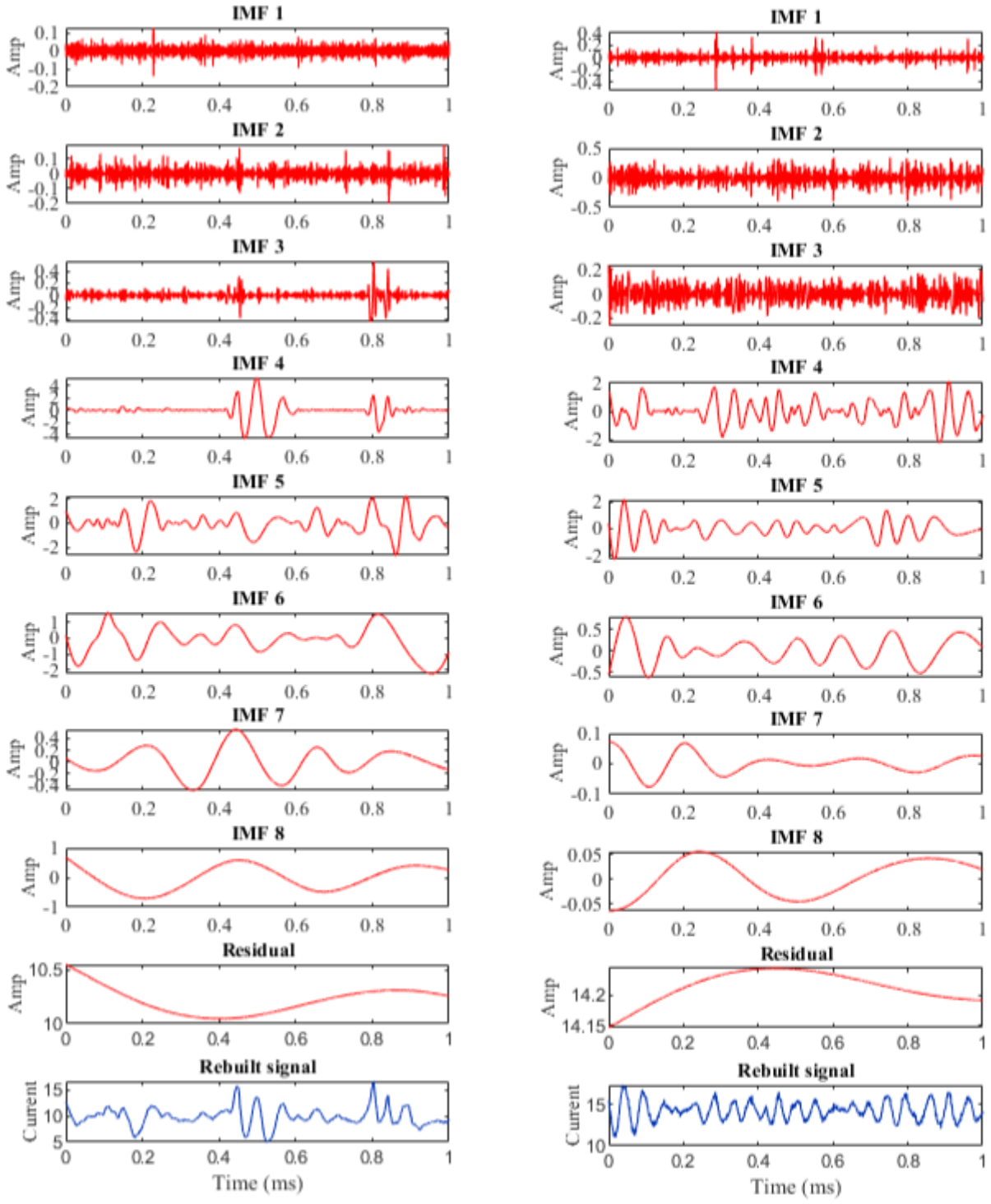

(a) EMD of the discharge current for xenon at 430 V (OP4). **(b) EMD of the discharge current for krypton at 450 V (OP4).**

Fig. 17 Empirical Mode Decomposition of the discharge current for xenon (a) and krypton (b). Intrinsic modes are shown in red and rebuilt signal in blue.

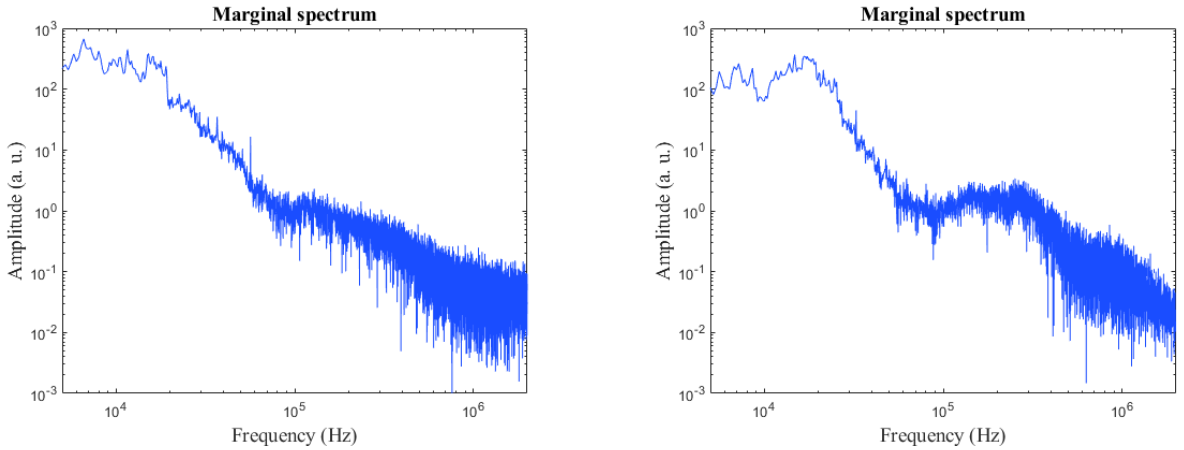

(a) Marginal spectrum for xenon - OP4.

(b) Marginal spectrum for krypton - OP4.

Fig. 18 Marginal spectrum of the discharge current time-series for xenon (a) and krypton (b).

VI. Conclusion

Time-series investigations on discharge oscillations were performed in the plume of the 5 kW-class PPS®Dual-EM Hall thruster from Safran running on xenon and krypton. The frequency dynamics of electron and discharge currents were systematically examined for each gas under varying discharge voltages and flow rates. The findings reveal a clear correlation between the breathing mode (BM) and discharge voltage. Specifically, as the discharge voltage increases, the BM frequency rises correspondingly. This increase is also associated with the emergence of ion transit-time instabilities (ITTs) and a pronounced amplification of BM oscillation amplitudes. Furthermore, the gases demonstrated distinct behaviors during the voltage range. Notably, krypton exhibited two distinct regimes, while xenon presented four regimes under the same magnetic field conditions. The second phase of the study focused on a time-frequency analysis of the measured currents. Initial analyses employed wavelet transforms across all selected operating points, followed by the application of the Huang-Hilbert transform to a representative point for each propellant. The time-series investigation revealed that xenon discharge currents displayed greater stability, characterized predominantly by the BM component, whereas krypton currents exhibited persistent high-frequency components. The wavelet transform analysis further identified intermittent phenomena and underscored the influence of discharge voltage on both low frequency (BM) and ITT oscillations behavior. Moreover, it illuminated specific local signal features during the decay phase of the BM oscillation, which were linked to the generation of ITTs and MHz-range (only with xenon) oscillations. Nevertheless, no strong correlation was highlighted between these two main oscillation modes in Hall thrusters. Future research could benefit from a more comprehensive investigation of the Huang-Hilbert Transform (HHT) including Hilbert spectra for each IMF (i.e. instataneous frequency and amplitude), alongside a detailed comparative analysis of the simultaneous behavior of discharge and ion currents using both wavelet and HHT techniques.

Acknowledgments

This work has been supported by the European Union in the frame of the Consortium for Hall Effect Orbital Propulsion System Medium Power project. This project has received funding from the European Union's Horizon Europe research and innovation program under grant agreement No 101004226.

References

[1] Dannenmayer, K., Kudrna, P., Tichý, M., and Mazouffre, S., "Time-resolved measurement of plasma parameters in the far-field plume of a low-power Hall effect thruster," *Plasma Sources Science and Technology*, Vol. 21, No. 5, 2012, p. 055020. https://doi.org/10.1088/0963-0252/21/5/055020.

[2] Dannenmayer, K., Kudrna, P., Tichý, M., and Mazouffre, S., "Time-Resolved measurements of plasma properties using electrostatic probes in the Cross-Field discharge of a hall effect thruster," *Contributions To Plasma Physics*, Vol. 53, No. 1, 2013, pp. 63–68. https://doi.org/10.1002/ctpp.201310011.

[3] Dannenmayer, K., Mazouffre, S., Kudrna, P., and Tichý, M., "The time-varying electron energy distribution function in the plume of a hall thruster," *Plasma Sources Science and Technology*, Vol. 23, No. 6, 2014, p. 065001. https://doi.org/10.1088/0963-0252/23/6/065001.

[4] Delavière—Delion, Q., Gaboriau, F., Fubiani, G., and Garrigues, L., "Experimental observation of low-frequency interactions at different scales and evidence of transit time oscillations in a Hall thruster: Spectral analysis," *Physics of Plasmas*, Vol. 31, No. 7, 2024. https://doi.org/10.1063/5.0206369, URL https://doi.org/10.1063/5.0206369.

[5] Mazouffre, S., and Delbosq, V., "Electron parameters in the plasma plume of a 5 kW Hall thruster firing with xenon and krypton," *In proceedings of the 38th International Electric Propulsion Conference*, 2024, pp. IEPC paper 2024–866. URL https://hal.science/hal-04666847.

[6] Tsikata, S., Cavalier, J., Héron, A., Honoré, C., Lemoine, N., Grésillon, D., and Coulette, D., "An axially propagating two-stream instability in the hall thruster plasma," *Physics of Plasmas*, Vol. 21, No. 7, 2014, p. 072116. https://doi.org/10.1063/1.4890025.

[7] Katz, I., Hofer, R. R., and Goebel, D. M., "Ion current in hall thrusters," *IEEE Transactions on Plasma Science*, Vol. 36, No. 5, 2008, pp. 2015–2024. https://doi.org/10.1109/tps.2008.2004219.

[8] Kim, S. W., and Gallimore, A. D., "Plume study of a 1.35-kW SPT-100 using an EXB probe," *Journal of Spacecraft and Rockets*, Vol. 39, No. 6, 2002, pp. 904–909. https://doi.org/10.2514/2.3897.

[9] Mazouffre, S., "Les propulseurs à plasma - une technologie spatiale d'avant-garde," *Reflets de la physique*, , No. 14, 2009, pp. 15–19. https://doi.org/10.1051/refdp/2009009.

[10] Choueiri, E. Y., "Plasma oscillations in Hall thrusters," *Physics of Plasmas*, Vol. 8, No. 4, 2001, pp. 1411–1426. https://doi.org/10.1063/1.1354644, URL https://doi.org/10.1063/1.1354644.

[11] Mazières, V., Gaboriau, F., Guglielmi, A., Laquerbe, V., Pascaud, R., and Pascal, O., "Broadband (kHz–GHz) characterization of instabilities in Hall thruster inside a metallic vacuum chamber," *Physics of Plasmas*, Vol. 29, No. 7, 2022. https://doi.org/10.1063/5.0090774, URL https://doi.org/10.1063/5.0090774.

[12] Boeuf, J.-P., "Tutorial: Physics and Modeling of hall thrusters," *Journal of Applied Physics*, Vol. 121, No. 1, 2017, p. 011101. https://doi.org/10.1063/1.4972269.

[13] Bœuf, J.-P., and Garrigues, L., "Low frequency oscillations in a stationary plasma thruster," *Journal of Applied Physics*, Vol. 84, No. 7, 1998, pp. 3541–3554. https://doi.org/10.1063/1.368529.

[14] Lipschultz, B., Hutchinson, I., LaBombard, B., and Wan, A., "Electric probes in plasmas," *J. Vac. Sci. Technol. A*, Vol. 4, 1986, pp. 1810–1816.

[15] Hutchinson, I. H., *Principles of Plasma Diagnostics*, Cambridge University Press, New York, 1987.

[16] Allen, J. E., "Probe Theory -The Orbital Motion Approach," *Physica Scripta*, Vol. 45, 1992, pp. 497–503.

[17] Demidov, V. I., Ratynskaia, S. V., and Rypdal, K., "Electric probes for plasmas: The link between theory and instrument," *Rev. Sci. Instrum.*, Vol. 73, 2002, pp. 3409–3439.

[18] Chen, F. F., "Lecture notes on Langmuir probe diagnostics," Mini-course on plasma diagnostics, IEEE-ICOPS meeting, Jeju, Korea, 2003.

[19] Merlino, R. L., "Understanding Langmuir probe current-voltage characteristics," *Am. J. Phys.*, Vol. 75, 2007, pp. 1078–1085.

[20] Dannenmayer, K., Kudrna, P., Tichý, M., and Mazouffre, S., "Measurement of plasma parameters in the far-field plume of a Hall effect thruster," *Plasma Sources Sci. Technol.*, Vol. 20, 2011, p. 065012.

[21] Tichý, M., "Plasma diagnostic by probes," Lecture notes for the Tomsk University, Russia, 2015.

[22] Riemann, K.-U., "The Bohm criterion and sheath formation," *J. Phys. D : Appl. Phys.*, Vol. 24, 1991, pp. 492–518.

[23] Franklin, R. N., "The plasma–sheath boundary region," *J. Phys. D : Appl. Phys.*, Vol. 36, 2003, pp. R309–320.

[24] Belinov, M. S., "The Child–Langmuir law and analytical theory of collisionless to collision-dominated sheaths," *Plasma Sources Sci. Technol.*, Vol. 18, 2009, p. 014005.

[25] Riemann, K.-U., "Plasma and sheath," *Plasma Sources Sci. Technol.*, Vol. 18, 2009, p. 014006.

[26] Belinov, M. S., "Space-charge sheath with ions accelerated into the plasma," *J. Phys. D: Appl. Phys.*, Vol. 43, 2010, p. 175203.

[27] Chabert, P., "What is the size of a floting sheath?" *Plasma Sources Sci. Technol.*, Vol. 23, 2014, p. 065042.

[28] Meyer, Y., Jaffard, S., and Orioul, O., "L'analyse par Ondelettes," *Pour la science*, 1987, pp. pp. 28–37.

[29] Bonhomme, G., Lemoine, N., Brochard, F., Lazurenko, A., Mazouffre, S., and Dudeck, M., "Characterization of high frequency plasma oscillations in a Hall effect thruster," *Proceedings of the 30th International Electric Propulsion Conference*, 2007.

[30] Torrence, C., and Compo, G. P., "A Practical Guide to Wavelet Analysis," *Bulletin of the American Meteorological Society*, Vol. 79, No. 1, 1998, pp. 61–78. https://doi.org/10.1175/1520-0477(1998)079, URL https://doi.org/10.1175/1520-0477(1998)079<0061:apgtwa>2.0.co;2.

[31] Farge, M., "Wavelet transforms and their applications to turbulence," *Annual Review of Fluid Mechanics*, Vol. 24, No. 1, 1992, pp. 395–457. https://doi.org/10.1146/annurev.fluid.24.1.395, URL https://doi.org/10.1146/annurev.fluid.24.1.395.

[32] Bultheel, A., "Learning to swim in a sea of wavelets," *Bulletin of the Belgian Mathematical Society - Simon Stevin*, Vol. 2, No. 1, 1995. https://doi.org/10.36045/bbms/1103408773, URL https://doi.org/10.36045/bbms/1103408773.

[33] Percival, D. B., and Walden, A. T., "Wavelet methods for time series analysis," *Choice Reviews Online*, Vol. 38, No. 08, 2001, pp. 38–4508. https://doi.org/10.5860/choice.38-4508, URL https://doi.org/10.5860/choice.38-4508.

[34] Lazurenko, A., Coduti, G., Mazouffre, S., and Bonhomme, G., "Dispersion relation of high-frequency plasma oscillations in Hall thrusters," *Physics of Plasmas*, Vol. 15, No. 3, 2008. https://doi.org/10.1063/1.2889424, URL https://doi.org/10.1063/1.2889424.

[35] Huang, N. E., Shen, Z., Long, S. R., Wu, M. C., Shih, H. H., Zheng, Q., Yen, N.-C., Tung, C. C., and Liu, H. H., "The empirical mode decomposition and the Hilbert spectrum for nonlinear and non-stationary time series analysis," *Proceedings of the Royal Society A Mathematical Physical and Engineering Sciences*, Vol. 454, No. 1971, 1998, pp. 903–995. https://doi.org/10.1098/rspa.1998.0193, URL https://doi.org/10.1098/rspa.1998.0193.

[36] Schmitt, F., Huang, Y., Lu, Z., and Liu, Y., "Propriétés multifractales dans l'espace de Hilbert : analyse de séries temporelles nonlinéaires et invariantes d'échelle utilisant la décomposition modale empirique et transformation de Hilbert," *Non Linéaire Publications*, 2011, pp. 163–168. https://doi.org/10.1063/1.1354644, URL https://doi.org/10.1063/1.1354644.

[37] Dätig, M., and Schlurmann, T., "Performance and limitations of the Hilbert–Huang transformation (HHT) with an application to irregular water waves," *Ocean Engineering*, Vol. 31, No. 14-15, 2004, pp. 1783–1834. https://doi.org/10.1016/j.oceaneng.2004.03.007, URL https://doi.org/10.1016/j.oceaneng.2004.03.007.

[38] Kurzyna, J., Makowski, K., Peradzynski, Z., Lazurenko, A., Mazouffre, S., Coduti, G., and Dudeck, M., "Current and Plasma Oscillation Inspection in PPS®-X000 HET Thruster - EMD Approach," *In proceedings of the 30th International Electric Propulsion Conference*, 2007, pp. IEPC paper 2007–23. URL https://electricrocket.org/IEPC/IEPC-2007-239.pdf.

[39] Kurzyna, J., Mazouffre, S., Lazurenko, A., Albarède, L., Bonhomme, G., Makowski, K., Dudeck, M., and Peradzyński, Z., "Spectral analysis of Hall effect thruster plasma oscillations based on the Empirical Mode Decomposition," *Phys. Plasmas*, Vol. 12, 2005.